Mon. Not. R. Astron. Soc. **340,** 73–90 (2003)

Implementations and tests of Godunov-type particle hydrodynamics

S.-H. Cha★† and A. P. Whitworth★
Department of Physics and Astronomy, Cardiff University, Cardiff CF2 3YB

Accepted 2002 November 8. Received 2002 October 1; in original form 2002 March 4

ABSTRACT

Godunov-type particle hydrodynamics (GPH) is described. GPH inherits many good features from smoothed particle hydrodynamics (SPH), but it uses a Riemann solver to obtain the hydrodynamic acceleration and the rate of change of the internal energy of each particle. The grid-free nature of GPH converts a multidimensional problem into a locally one-dimensional problem, so that one only has to solve a one-dimensional Riemann problem, even in a globally three-dimensional situation. By virtue of the Riemann solver, it is unnecessary to introduce artificial viscosity in GPH. We have derived four different versions of GPH, and have performed a von Neumann stability analysis to understand the nature of GPH. GPH is stable for all wavelengths, while SPH is unstable for certain wavelengths. We have also performed eight tests in order to evaluate the performance of GPH. The results show that GPH can describe shock waves without artificial viscosity and prevents particle penetration. Furthermore, GPH shows better performance than SPH in a test involving velocity shear. GPH is easily implemented from SPH by simple replacement of the artificial viscosity with a Riemann solver, and appears to have some useful advantages over standard SPH.

Key words: hydrodynamics – methods: numerical.

1 INTRODUCTION

Smoothed particle hydrodynamics (SPH) (Gingold & Monaghan 1977; Lucy 1977) is a grid-free, fully three-dimensional Lagrangian method, and therefore it is a powerful technique for simulating irregularly shaped gravitational hydrodynamics. The principle of SPH is that a 'smoothed particle' can represent the physical properties of a fluid element. The 'smoothed particles' are made by averaging the physical quantities of the fluid elements over an extended volume using a kernel function.

The equations of SPH can be derived directly from the equations of Lagrangian hydrodynamics:

$$\frac{\mathrm{D}\rho}{\mathrm{D}}t = -\rho\nabla\cdot\boldsymbol{v}, \tag{1}$$

$$\frac{\mathrm{D}\boldsymbol{v}}{\mathrm{D}t} = -\frac{1}{\rho}\nabla P, \tag{2}$$

$$\frac{\mathrm{D}u}{\mathrm{D}t} = -\frac{P}{\rho}\nabla\cdot\boldsymbol{v}, \tag{3}$$

where $\mathrm{D}/\mathrm{D}t \equiv \partial/\partial t + \boldsymbol{v}\cdot\nabla$, u is the specific internal energy and all other variables have their usual meanings. There are various forms for the equations of SPH that exactly conserve momentum and total energy. However, we will treat only the two most widely used forms, and these two forms will be used in the implementation of Godunov-type particle hydrodynamics (GPH). The first form (SPH 1) is

$$\frac{\Delta\boldsymbol{v}_i}{\Delta t} = -\sum_j m_j\left(\frac{P_i}{\rho_i^2}+\frac{P_j}{\rho_j^2}+\Pi_{ij}\right)\nabla_i W(\boldsymbol{r}_i-\boldsymbol{r}_j;h_{ij}), \tag{4}$$

$$\frac{\Delta u_i}{\Delta t} = \frac{1}{2}\sum_j m_j\left(\frac{P_i}{\rho_i^2}+\frac{P_j}{\rho_j^2}+\Pi_{ij}\right)(\boldsymbol{v}_i-\boldsymbol{v}_j)\cdot\nabla_i W(\boldsymbol{r}_i-\boldsymbol{r}_j;h_{ij}), \tag{5}$$

and the second form (SPH 2) is

$$\frac{\Delta\boldsymbol{v}_i}{\Delta t} = -2\sum_j m_j\left(\frac{\sqrt{P_iP_j}}{\rho_i\rho_j}+\frac{1}{2}\Pi_{ij}\right)\nabla_i W(\boldsymbol{r}_i-\boldsymbol{r}_j;h_{ij}), \tag{6}$$

$$\frac{\Delta u_i}{\Delta t} = \sum_j m_j\left(\frac{\sqrt{P_iP_j}}{\rho_i\rho_j}+\frac{1}{2}\Pi_{ij}\right)\left(\boldsymbol{v}_i-\boldsymbol{v}_j\right)\cdot\nabla_i W(\boldsymbol{r}_i-\boldsymbol{r}_j;h_{ij}), \tag{7}$$

where $\nabla_i = \mathrm{d}/\mathrm{d}\boldsymbol{r}_i$, $h_{ij}=(h_i+h_j)/2$ and W is a kernel function. Here Π_{ij} is an artificial viscosity term that will be explained later. The *i*–*j* symmetric form of equations (4)–(7) guarantees the conservation of linear momentum, angular momentum and total energy.

Many different kernel functions have been proposed (Gingold & Monaghan 1977, 1982; Wood 1981; Monaghan & Lattanzio 1984; Monaghan 1992). The spatial accuracy of SPH is determined

★E-mail: cha@astro.umontreal.ca (S-HC); Anthony. Whitworth@astro.cf.ac.uk (APW)
†Present address: Département de Physique, Université de Montréal, C.P. 6128, Succ. Centre-ville, Montréal, Québec, H3C 3J7, Canada.

© 2003 RAS

Downloaded from https://academic.oup.com/mnras/article/340/1/73/1130605 by guest on 12 November 2025

by the kernel, and second-order accuracy is achieved by using spherically symmetric kernels. However, equations (4)–(7) have only first-order accuracy in time, so a two-step evolution algorithm is needed, such as the predictor–corrector or the second-order Runge–Kutta method.

1.1 Artificial viscosity and particle penetration

SPH uses an artificial viscosity, Π_{ij}, optimized to treat shock waves. It is composed of linear and quadratic terms, and is only turned on when two particles are approaching:

$$\Pi_{ij} = \begin{cases} \dfrac{-\alpha \bar{c}_{ij}\mu_{ij} + \beta\mu_{ij}^2}{\bar{\rho}_{ij}} & \text{when } \mu_{ij} < 0, \\ 0 & \text{otherwise,} \end{cases} \tag{8}$$

where $\mu_{ij} = (h_{ij}\boldsymbol{v}_{ij}\cdot\boldsymbol{r}_{ij})/(r_{ij}^2 + 0.01h_{ij}^2)$, $\boldsymbol{v}_{ij} = \boldsymbol{v}_i - \boldsymbol{v}_j$, $\boldsymbol{r}_{ij} = \boldsymbol{r}_i - \boldsymbol{r}_j$, $\bar{c}_{ij} = \frac{1}{2}(c_i + c_j)$, $\bar{\rho}_{ij} = \frac{1}{2}(\rho_i + \rho_j)$ and c is the speed of sound. α and β in equation (8) are free parameters to regulate the strength of artificial viscosity. The term $0.01h_{ij}^2$ in the denominator of Π_{ij} is to avoid singularity when $\boldsymbol{r}_i \simeq \boldsymbol{r}_j$, but it is not critical since normally $|\boldsymbol{r}_i - \boldsymbol{r}_j| \gtrsim h_{ij}$ (Whitehurst 1995; Monaghan 1997).

In standard SPH, some form of artificial viscosity is essential for treating shock waves. However, even with artificial viscosity there can be an unacceptable level of particle penetration. Additionally, the commonly used form of artificial viscosity defined in equation (8) corrupts the simulation of flows in which there is velocity shear (for example, differentially rotating discs or obliquely colliding clouds) by giving rise to a very large effective shear viscosity. There have been several attempts to refine the artificial viscosity defined in equation (8) so as to avoid these problems. Monaghan (1989) proposed correcting the velocity of an individual particle by adding the kernel-averaged mean of the relative velocities of its neighbours. This improved the treatment of shocks. Balsara (1995) introduced a coefficient that greatly reduced μ_{ij} unless $(-\nabla\cdot\boldsymbol{v})$ was large, positive and much greater than $|\nabla\times\boldsymbol{v}|$. This alleviated the shear problem in some situations. Watkins et al. (1996) solved the Navier–Stokes equations directly using less noisy forms of $(\nabla\times\boldsymbol{v})_i$ and $(\nabla\cdot\boldsymbol{v})_i$. Morris & Monaghan (1997) explored a time-dependent coefficient α, which became large wherever $(-\nabla\cdot\boldsymbol{v})$ was (or had recently been) large, and then quickly decayed back to a small residual value. However, all of these attempts have met with only partial success.

Evidently, the best method to avoid the side-effects of artificial viscosity in SPH is to eliminate the need for artificial viscosity. GPH does not need artificial viscosity, and can describe shock waves. Therefore, the side-effects of artificial viscosity in SPH do not appear in GPH.

1.2 The stability of SPH

Von Neumann stability analysis for SPH (Monaghan 1989; Balsara 1995; Morris 1996a,b) shows that it is unstable to negative stress, especially at the critical wavenumber $\pi/\Delta x$ (where Δx is the mean distance between particles). Artificial viscosity damps this instability, but cannot suppress the instability completely.

The instability can also be reduced by a suitable choice of kernel. Morris (1996a,b) suggests that higher-order kernels should reduce the instability better than standard kernels such as the exponential (Wood 1981), Gaussian (Gingold & Monaghan 1977), super-Gaussian (Gingold & Monaghan 1982; Monaghan 1992) and M4 (Monaghan & Lattanzio 1984) kernels.

We will present the von Neumann stability analyses for SPH and GPH in Section 4, and will show that GPH is stable for all wavelengths.

1.3 Godunov-type particle hydrodynamics

GPH is a hybrid scheme combining SPH with a Godunov-type upwind scheme. It was initially suggested by Inutsuka (1994, 1999 and unpublished); Inutsuka & Imaeda (2001) (see also Cha 2002). Inutsuka proposed two different methods. We call the first one 'the imaginary particle method' (Inutsuka 1994 and unpublished) because it uses imaginary particles to estimate the hydrodynamic force and the rate of change of the internal energy. The second one is an improved method to solve the Riemann problem between each pair of interacting particles (Inutsuka 1999; Inutsuka & Imaeda 2001). A detailed description and the results of many tests for each version of GPH are presented in Cha (2002).

1.4 Plan of this paper

We analyse the treatment of shock waves by numerical schemes in Section 2 and we describe the implementation of GPH in Section 3. The von Neumann stability analyses for SPH and GPH are presented in Section 4. We have performed eight tests, and the results are presented in Section 5. The discussion and summary are given in Section 6.

2 SHOCK WAVES AND DISSIPATION IN THE NUMERICAL SCHEME

Shock waves are a common phenomenon in astrophysical hydrodynamics. Once a shock wave occurs, all physical quantities – such as density, pressure and velocity – change rapidly across the shock front. In reality, the thickness of a shock layer is a few times the mean free path of the gas particles at the temperature of the shock. The thickness of the shock layer is normally negligible compared with the size of the whole system, and so the shock front is in effect a discontinuity in the physical quantities. Equations (1)–(3) are able to describe continuous regions (i.e. regions in which all physical quantities change smoothly), but they have great difficulty in the description of discontinuities such as shock waves. Another characteristic of a shock wave is that it increases the entropy of the gas, while other discontinuous structures (i.e. rarefaction waves and contact discontinuities) are isentropic (Landau & Lifshitz 1998).

Various methods have been proposed to treat shock waves. One of them is artificial viscosity, which was proposed by von Neumann & Richtmyer (1950). The artificial viscosity of von Neumann & Richtmyer is quadratic in the velocity divergence and consequently the shock thickness is approximately independent of the shock strength. Von Neumann & Richtmyer also proved that a shock smeared out by artificial viscosity travels with exactly the same speed as a discontinuous one would, and produces exactly the same entropy increase (Richtmyer & Morton 1967).

SPH uses a slightly different artificial viscosity (e.g. Monaghan 1992). The artificial viscosity normally used in SPH is composed of both linear and quadratic terms in the velocity divergence. The linear and quadratic terms are sensitive to small and large (negative) velocity divergence, respectively. However, although artificial viscosity is a good method for treating shock waves, it has some undesirable side-effects in systems with velocity shear. Furthermore, artificial viscosity sometimes permits particle penetration in SPH (Monaghan 1989).

Downloaded from https://academic.oup.com/mnras/article/340/1/73/1130605 by guest on 12 November 2025

Godunov (1959) suggested a new method for one-dimensional hydrodynamic problems with shock waves. The history of the Godunov scheme is well described in Hirsch (1989, 1997), van Leer (1999) and Godunov (1999). The Godunov method is based on Lagrangian hydrodynamics, and works by using a Riemann solver to calculate a numerical flux at the border of each cell. By virtue of the Riemann solver, a time-independent, space-centred numerical flux is obtained. Extra numerical dissipation is not needed, even if there are shock waves in the system, because the Riemann solver can exactly describe all the waves (i.e. shock waves and rarefaction waves) that occur between two adjacent fluids.

3 IMPLEMENTATION OF GPH

3.1 The equations of GPH

The simplest way to combine SPH and the Riemann problem is to replace P_i and P_j with P^*, the resultant pressure of the Riemann solver, in equations (4)–(7). This replacement will not affect the conservation of total momentum and energy (Cha 2002). The replacement can be made in either of the two widely used forms of SPH described in equations (4)–(7), to give

Case 1 (from SPH 1):

$$\frac{\Delta \boldsymbol{v}_i}{\Delta t} = -\sum_j m_j P^* \left(\frac{1}{\rho_i^2} + \frac{1}{\rho_j^2}\right) \nabla_i W(\boldsymbol{r}_i - \boldsymbol{r}_j; h_{ij}), \tag{9}$$

$$\frac{\Delta u_i}{\Delta t} = \frac{1}{2}\sum_j m_j P^* \left(\frac{1}{\rho_i^2} + \frac{1}{\rho_j^2}\right) (\boldsymbol{v}_i - \boldsymbol{v}_j) \cdot \nabla_i W(\boldsymbol{r}_i - \boldsymbol{r}_j; h_{ij}). \tag{10}$$

Case 2 (from SPH 2):

$$\frac{\Delta \boldsymbol{v}_i}{\Delta t} = -2\sum_j m_j \frac{P^*}{\rho_i \rho_j} \nabla_i W(\boldsymbol{r}_i - \boldsymbol{r}_j; h_{ij}), \tag{11}$$

$$\frac{\Delta u_i}{\Delta t} = \sum_j m_j \frac{P^*}{\rho_i \rho_j} (\boldsymbol{v}_i - \boldsymbol{v}_j) \cdot \nabla_i W(\boldsymbol{r}_i - \boldsymbol{r}_j; h_{ij}). \tag{12}$$

Note that there is no artificial viscosity term in equations (9)–(12).

Inutsuka & Imaeda (2001) have proposed new formulations for SPH. More recently, Monaghan (2002) and Springel & Hernquist (2002) have derived the same formulations. The replacements can also be made in these new formulations, to give

Case 3:

$$\frac{\Delta \boldsymbol{v}_i}{\Delta t} = -\sum_j m_j P^* \left[\frac{1}{\rho_i^2}\frac{\partial}{\partial \boldsymbol{r}_i} W(\boldsymbol{r}_i - \boldsymbol{r}_j, h_i) + \frac{1}{\rho_j^2}\frac{\partial}{\partial \boldsymbol{r}_i} W(\boldsymbol{r}_i - \boldsymbol{r}_j, h_j)\right], \tag{13}$$

$$\frac{\Delta u_i}{\Delta t} = \sum_j m_j P^* \left(\boldsymbol{v}^* - \dot{\boldsymbol{r}}_i^*\right) \left[\frac{1}{\rho_i^2}\frac{\partial}{\partial \boldsymbol{r}_i} W(\boldsymbol{r}_i - \boldsymbol{r}_j, h_i) + \frac{1}{\rho_j^2}\frac{\partial}{\partial \boldsymbol{r}_i} W(\boldsymbol{r}_i - \boldsymbol{r}_j, h_j)\right]. \tag{14}$$

Case 4:

$$\frac{\Delta \boldsymbol{v}_i}{\Delta t} = -\sum_j m_j \int \frac{P^*}{\rho^2(\boldsymbol{r})} \left(\frac{\partial}{\partial \boldsymbol{r}_i} - \frac{\partial}{\partial \boldsymbol{r}_j}\right) \times W(\boldsymbol{r} - \boldsymbol{r}_i, h) W(\boldsymbol{r} - \boldsymbol{r}_j, h)\, \mathrm{d}\boldsymbol{r}, \tag{15}$$

$$\frac{\Delta u_i}{\Delta t} = \sum_j m_j \left(\boldsymbol{v}^* - \dot{\boldsymbol{r}}_i^*\right) \int \frac{P^*}{\rho^2(\boldsymbol{r})} \left(\frac{\partial}{\partial \boldsymbol{r}_i} - \frac{\partial}{\partial \boldsymbol{r}_j}\right) \times W(\boldsymbol{r} - \boldsymbol{r}_i, h) W(\boldsymbol{r} - \boldsymbol{r}_j, h)\, \mathrm{d}\boldsymbol{r}, \tag{16}$$

where $\boldsymbol{v}^*$ is the resultant velocity of the Riemann solver and $\dot{\boldsymbol{r}}_i^*$ is the time-averaged value of $\dot{\boldsymbol{r}}_i$ [$\equiv (\dot{\boldsymbol{r}}_i^n + \dot{\boldsymbol{r}}_i^{n+1})/2$]. The derivation of equations (13)–(16) is given in Inutsuka & Imaeda (2001), Monaghan (2002), Springel & Hernquist (2002), and described more fully in Cha (2002).

3.2 The iterative Riemann solver

The Riemann solver determines the overall efficiency (accuracy and speed) of the Godunov scheme. Although there are many numerical Riemann solvers (e.g. Toro 1999 and references therein), we have used the one proposed by van Leer (1997). It is faster than the traditional method of Godunov (e.g. Richtmyer & Morton 1967). We briefly describe the Riemann solver of van Leer (1997) here, because it is at the heart of GPH.

First, the Lagrangian shock speed ($\equiv W$) is defined by

$$W = \begin{cases} C\left(1 + \dfrac{\gamma+1}{2\gamma}\dfrac{P^* - P}{P}\right)^{1/2} & \text{when } P^* \geqslant P, \\ \dfrac{\gamma-1}{2\gamma}\dfrac{1 - P^*/P}{1 - (P^*/P)^{(\gamma-1)/2\gamma}} C & \text{otherwise,} \end{cases} \tag{17}$$

where γ is the ratio of specific heats and C is the Lagrangian speed of sound ($\equiv \sqrt{\gamma P \rho}$). Post-shock values are indicated by an asterisk in equation (17). Next, the tangential slope, $Z(\equiv \frac{\mathrm{d}P^*}{\mathrm{d}v^*})$ is calculated from the Lagrangian shock speed,

$$Z = \begin{cases} \dfrac{2W^2}{W^2 + C^2} W & \text{when } P^* \geqslant P, \\ C(P^*/P)^{[1-(\gamma-1)/2\gamma]} & \text{otherwise.} \end{cases} \tag{18}$$

P^* is then found by iteration using

$$P^{*(n+1)} = P^{*(n)} - \frac{Z_b^{(n)} Z_a^{(n)} \left[v_a^{*(n)} - v_b^{*(n)}\right]}{Z_b^{(n)} + Z_a^{(n)}} \tag{19}$$

until $P^{*(n+1)}$ differs by less than 1.5 percent from $P^{*(n)}$. Here the subscripts a and b denote two adjacent fluids. At every iteration, v^* should be updated by

$$v_a^{*(n)} = v_a + \frac{P^{*(n)} - P_a}{W_a}, \tag{20}$$

$$v_b^{*(n)} = v_b - \frac{P^{*(n)} - P_b}{W_b}. \tag{21}$$

The final velocity can be derived from

$$v^* = \frac{Z_b v_b^* + Z_a v_a^*}{Z_b + Z_a}. \tag{22}$$

An initial estimate of P^* is needed to start the iteration. It is given by

$$P^{*(1)} = \frac{C_a P_b + C_b P_a - C_a C_b (v_a - v_b)}{C_a + C_b}. \tag{23}$$

In order to reduce numerical oscillation, P^* is iterated only if $P^{*(1)}$ differs by more than 1 percent from P_a and P_b, and in order to prevent divergence of the iteration, a pressure protection is also used (van Leer 1997). The divergence of iterative Riemann solvers will be discussed further in Section 5.5.

Downloaded from https://academic.oup.com/mnras/article/340/1/73/1130605 by guest on 12 November 2025

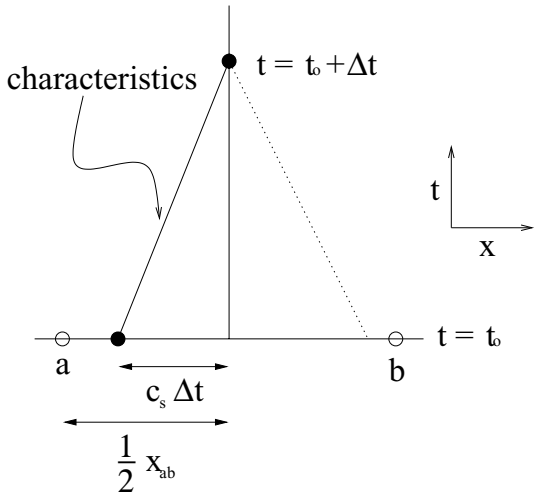

Figure 1. A diagram to show the concept of an upstream scheme. The Riemann invariant is constant along the characteristics [solid (or dotted) line], so the two filled circles connected by the solid line have the same physical quantities. The upstream scheme uses the value at the filled circle rather than the arithmetic mean of values at a and b.

3.3 The isothermal Riemann solver

For an isothermal gas, the non-iterative Riemann solver proposed by Balsara (1994) can be used, and this is obviously faster than an iterative Riemann solver.

The post-shock velocity, v^* is given by

$$v^* = v_{\rm L} - \frac{P^* - c_{\rm s}^2\rho_{\rm L}}{\sqrt{P^*\rho_{\rm L}}}, \tag{24}$$

$$= v_{\rm R} + \frac{P^* - c_{\rm s}^2\rho_{\rm R}}{\sqrt{P^*\rho_{\rm R}}}. \tag{25}$$

A quadratic for $\sqrt{P^*}$ is derived by eliminating v^* between equations (24) and (25),

$$P^* - (v_{\rm L} - v_{\rm R})X\sqrt{P^*} - c^2X(\sqrt{\rho_{\rm L}} + \sqrt{\rho_{\rm R}}) = 0, \tag{26}$$

where $X = \sqrt{\rho_{\rm L}}\sqrt{\rho_{\rm R}}/(\sqrt{\rho_{\rm L}} + \sqrt{\rho_{\rm R}})$. The positive solution of the quadratic is accepted, and is given by

$$P^* = \left(\frac{1}{2}\right)^2 \Big[X(v_{\rm L} - v_{\rm R}) + \sqrt{X^2(v_{\rm L} - v_{\rm R})^2 + 4c_{\rm s}^2X(\sqrt{\rho_{\rm L}} + \sqrt{\rho_{\rm R}})}\Big]^2. \tag{27}$$

v^* can then be derived from equation (24) (or equation 25).

3.4 A simple comparison between the equations of SPH and GPH

The physical interpretation of the replacements in equations (9)–(16) is simple. The hydrodynamic motion of particle a is determined by the pressure distribution of its environment.[1] GPH uses the evolved value, P^* (at $t = t_0 + \Delta t$) instead of P_a and P_b (at $t = t_0$). Fig. 1 shows the concept of upstream schemes such as GPH. If the pressure varies linearly from $\boldsymbol{r}_a$ to $\boldsymbol{r}_b$, P^* can be expressed by $C_1P_a + (1 - C_1)P_b$, where C_1 is a constant. To see the difference between SPH and GPH, the equations of motion are linearized.

The linearized form of $P^*(\frac{1}{\rho_a} + \frac{1}{\rho_b})$ is obtained by substituting $P = P_0 + \delta P$ and $\rho = \rho_0 + \delta\rho$ to give

$$P^*\left(\frac{1}{\rho_a} + \frac{1}{\rho_b}\right) \simeq 2\frac{P_0}{\rho_0} + 2C_1\frac{\delta P_a}{\rho_0^2} + 2(1 - C_1)\frac{\delta P_b}{\rho_0^2} - 2P_0\frac{\delta\rho_a + \delta\rho_b}{\rho_0^3}. \tag{28}$$

We can compare this with the linearized form of SPH,

$$\frac{P_a}{\rho_a^2} + \frac{P_b}{\rho_b^2} \simeq 2\frac{P_0}{\rho_0} + \frac{\delta P_a + \delta P_b}{\rho_0^2} - 2P_0\frac{\delta\rho_a + \delta\rho_b}{\rho_0^3}. \tag{29}$$

The only difference between equations (28) and (29) is the middle term. The difference is

$$\Delta_{\rm SPH,GPH} = (2C_1 - 1)\frac{\delta P_a - \delta P_b}{\rho_0^2}. \tag{30}$$

If $C_1 = \frac{1}{2}$, i.e. P^* is the arithmetic mean of P_a and P_b, then the motion equation of GPH is identical to that of SPH. Another special case is $P_a = P_b$. In this case, there is no hydrodynamic acceleration between a and b, and GPH and SPH describe the same situation.

4 STABILITY ANALYSES

In order to understand GPH more precisely, the von Neumann stability analysis (e.g. Richtmyer & Morton 1967) has been applied to isothermal hydrodynamics. The von Neumann stability analysis was originally applied to finite-difference methods (FDMs), and subsequently also to SPH (Monaghan 1989; Balsara 1995; Morris 1996a).

The stability analysis presented here is for case 1 (SPH 1). However, the linearized forms of cases 1–3 are identical, so there are no differences in the stability analyses of cases 1–3. It is unclear how to linearize case 4, but we presume that there are no major differences between the stability analyses of cases 1–3 and 4. We will explain the reason for this presumption in Section 5.1.

First of all, the stability analysis of isothermal SPH without artificial viscosity will be presented for reference. We will then repeat the analysis for the cases of SPH with artificial viscosity, and GPH.

4.1 SPH without artificial viscosity

For simplicity, we initially consider a system where all particles have the same mass ($\equiv M$) and are equally spaced:

$$x_a = a\Delta x, \tag{31}$$

$$\rho_a = \rho_0, \tag{32}$$

$$v_a = 0, \tag{33}$$

$$u_a = u_0. \tag{34}$$

A small perturbation is then added to the system,

$$x_a = a\Delta x + X\mathrm{e}^{\mathrm{i}\phi_a} \quad (\equiv a\Delta x + \delta x_a), \tag{35}$$

$$\rho_a = \rho_0 + R\mathrm{e}^{\mathrm{i}\phi_a} \quad (\equiv \rho_0 + \delta\rho_a), \tag{36}$$

$$v_a = 0 + V\mathrm{e}^{\mathrm{i}\phi_a} \quad (\equiv 0 + \delta v_a), \tag{37}$$

$$u_a = u_0 + U\mathrm{e}^{\mathrm{i}\phi_a} \quad (\equiv u_0 + \delta u_a), \tag{38}$$

[1] We will use particle indices a and b instead of i and j in Sections 3.4 and 4, because the particle index i can be confused with the imaginary number i.

Downloaded from https://academic.oup.com/mnras/article/340/1/73/1130605 by guest on 12 November 2025

where $\phi_a = \kappa a \Delta x - \omega t$, and κ and ω are, respectively, the wavenumber and angular velocity of the initial perturbation.

The equations of SPH without artificial viscosity are given by

$$\frac{\mathrm{d}x_a}{\mathrm{d}t} = v_a, \tag{39}$$

$$\rho_a = M \sum_b W_{a,b}, \tag{40}$$

$$\frac{\mathrm{d}v_a}{\mathrm{d}t} = -M \sum_b \left(\frac{P_a}{\rho_a^2} + \frac{P_b}{\rho_b^2} \right) \frac{\partial W_{a,b}}{\partial x_a}, \tag{41}$$

where $W_{a,b}$ is $W(x_a - x_b, h)$ and all h-values are assumed constant. To close the system, the equation of state,

$$P = c_\mathrm{s}^2 \rho \tag{42}$$

is used. Here c_s is the isothermal speed of sound.

When linearized, equations (39)–(41) reduce to

$$X = \frac{V}{\omega}\mathrm{i}, \tag{43}$$

$$R = MX \sum_b (1 - \mathrm{e}^{\mathrm{i}\phi_{b-a}}) \frac{\partial W_{a,b}}{\partial x_a}, \tag{44}$$

$$V = \frac{M}{\mathrm{i}\omega} \frac{c_\mathrm{s}^2}{\rho_0} \sum_b \left[-\frac{R}{\rho_0} (1 + \mathrm{e}^{\mathrm{i}\phi_{b-a}}) \frac{\partial W_{a,b}}{\partial x_a} + 2X(1 - \mathrm{e}^{\mathrm{i}\phi_{b-a}}) \frac{\partial^2 W_{a,b}}{\partial x_a^2} \right], \tag{45}$$

where $\phi_{b-a} = \kappa(b-a)\,\Delta x$. The dispersion relation for SPH without artificial viscosity is derived from the combination of equations (43)–(45):

$$\omega_\mathrm{SPH}^2 = M \frac{c_\mathrm{s}^2}{\rho_0} \sum_b \left\{ -\frac{M}{\rho_0} \left[\sum_b (1 - \mathrm{e}^{\mathrm{i}\phi_{b-a}}) \frac{\partial W_{a,b}}{\partial x_a} \right] \times (1 + \mathrm{e}^{\mathrm{i}\phi_{b-a}}) \frac{\partial W_{a,b}}{\partial x_a} + 2(1 - \mathrm{e}^{\mathrm{i}\phi_{b-a}}) \frac{\partial^2 W_{a,b}}{\partial x_a^2} \right\}. \tag{46}$$

Morris (1996a) considers three different methods for estimating $\sum_b [1 \pm \mathrm{e}^{\mathrm{i}(b-a)\kappa\Delta x}]$ ($\partial^n W_{a,b}/\partial x_\mathrm{a}^\mathrm{n}$), but we have used only the two methods given below.

(i) The simple integral approximation, i.e. $\sum_a f(a) \simeq \int_{-\infty}^{\infty} f(x)\,\mathrm{d}x$,

$$\sum_b \left[1 \pm \mathrm{e}^{\mathrm{i}(b-a)\kappa\Delta x} \right] \frac{\partial^n W_{a,b}}{\partial x_a^n} \simeq \frac{\pm(\mathrm{i}\kappa)^n}{\Delta x} \hat{W}(b-a, k), \tag{47}$$

where $\hat{W}(b-a, k)$ is the Fourier transform of $W_{a,b}$.

(ii) Direct summation with an even kernel function gives

$$\sum_b \left[1 \pm \mathrm{e}^{\mathrm{i}(b-a)\kappa\Delta x} \right] \frac{\partial W_{a,b}}{\partial x_a} \simeq \pm \sum_b \mathrm{i} \sin[(b-a)\kappa\Delta x] \frac{\partial W_{a,b}}{\partial x_a}, \tag{48}$$

$$\sum_b \left[1 \pm \mathrm{e}^{\mathrm{i}(b-a)\kappa\Delta x} \right] \frac{\partial^2 W_{a,b}}{\partial x_a^2} \simeq \sum_b \{1 \pm \cos[(b-a)\kappa\Delta x]\} \frac{\partial^2 W_{a,b}}{\partial x_a^2}. \tag{49}$$

The simple integral approximation is not exact, but it is useful when one wants to know the asymptotic behaviour of equation (46). In the long-wavelength limit (i.e. $\kappa \to 0$), $\hat{W}(b-a, k)$ approaches unity, and equation (46) becomes

$$\omega_\mathrm{SPH}^2 = c_\mathrm{s}^2 \kappa^2, \tag{50}$$

where we assume $\rho\Delta x \simeq M$. This is identical to the dispersion relation of a sound wave.

To investigate equation (46) more exactly, direct summation is applied. We have used the M4 kernel in the analyses. In this case, equation (46) becomes

$$\omega_\mathrm{SPH}^2 = -\left(\frac{M c_\mathrm{s}}{\rho} \right)^2 \left\{ \sum_b \sin[(b-a)\kappa\Delta x] \frac{\partial W_{a,b}}{\partial x_a} \right\}^2 + \frac{2M c_\mathrm{s}^2}{\rho_0} \sum_b \{1 - \cos[(b-a)\kappa\Delta x]\} \frac{\partial^2 W_{a,b}}{\partial x_a^2}. \tag{51}$$

In order to understand equation (51), we have to recall the initial perturbation, which is of the form $\mathrm{e}^{\mathrm{i}(\kappa x - \omega t)}$. So the wavelength ($\equiv \lambda$), period ($\equiv T$) and speed of propagation ($\equiv v$) of the initial perturbation are given by

$$\lambda = \frac{2\pi}{\kappa}, \tag{52}$$

$$T = \frac{2\pi}{\omega}, \tag{53}$$

$$v = \frac{\lambda}{T} = \frac{\omega}{\kappa} \quad (\equiv c_\mathrm{s}), \tag{54}$$

respectively. If the angular velocity, ω is changed to ω' ($\equiv \omega_\mathrm{R} + \mathrm{i}\omega_\mathrm{I}$), the change to the initial wave is given by

$$\mathrm{e}^{\mathrm{i}(\kappa x - \omega_\mathrm{R} t - \mathrm{i}\omega_\mathrm{I} t)} = \mathrm{e}^{\omega_\mathrm{I} t} \mathrm{e}^{\mathrm{i}(\kappa x - \omega_\mathrm{R} t)}. \tag{55}$$

The imaginary part, ω_I, gives the 'change of amplitude', i.e. the error in the amplitude,

$$E_R = \mathrm{e}^{\omega_\mathrm{I} t}. \tag{56}$$

The real part, ω_R, gives the 'change of phase', i.e. the error in the phase,

$$E_\Phi = \frac{|\omega - \omega_\mathrm{R}|}{\omega}. \tag{57}$$

If ω_I is smaller than 0, the error in the amplitude will decrease.

Equation (51) has only a phase error because there is only a real term. Fig. 2 shows E_Φ from equation (51). SPH without artificial viscosity is always stable because w_SPH^2 is positive for all κ and h.

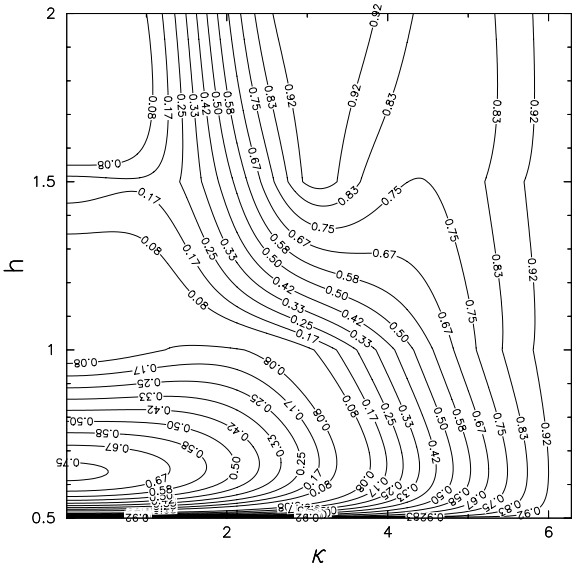

Figure 2. Phase error contours for isothermal SPH without artificial viscosity. There is no unstable region at any wavelength because ω^2_SPH is always positive. $M = 1$ and $\Delta x = 1$ are used in this plot. The number of neighbours is three to five in the range of $1.0 < h < 1.5$. With these h-values, E_Φ approaches 0 in the long-wavelength limit.

Downloaded from https://academic.oup.com/mnras/article/340/1/73/1130605 by guest on 12 November 2025

4.2 SPH with artificial viscosity

Although the artificial viscosity of SPH is composed of both a linear term (the α-term) and a quadratic term (the β-term), only the α-term [$\equiv \frac{2\alpha c_s h}{\rho_a+\rho_b}\frac{(v_a-v_b)(x_a-x_b)}{(x_a-x_b)^2+0.01h^2}$] is used when we derive the dispersion relation of SPH with artificial viscosity, because the β-term is of second order. Also, we follow Morris (1996a) in applying artificial viscosity to both approaching and receding pairs of particles.

The dispersion relation for this case is given by

$$\omega^2_{\rm SPH,AV} = M\frac{c_s^2}{\rho_0}\sum_b\left\{-\frac{M}{\rho_0}\left[\sum_b(1-{\rm e}^{{\rm i}\phi_{b-a}})\frac{\partial W_{a,b}}{\partial x_a}\right]\right.$$
$$\left.\times(1+{\rm e}^{{\rm i}\phi_{b-a}})\frac{\partial W_{a,b}}{\partial x_a}+2(1-{\rm e}^{{\rm i}\phi_{b-a}})\frac{\partial^2 W_{a,b}}{\partial x_a^2}\right\}$$
$$+M\frac{c_s}{\rho_0}\alpha h\sum_b\frac{1-{\rm e}^{{\rm i}\phi_{b-a}}}{(b-a)\Delta x}\frac{\partial W_{a,b}}{\partial x_a}\omega\,{\rm i}. \qquad (58)$$

Equation (58) can be expressed in a more concise form by substituting for $\omega^2_{\rm SPH}$ from equation (51)

$$\omega^2_{\rm SPH,AV}\ -{\rm i}M\frac{c_s}{\rho_0}\alpha h\sum_b\left\{\frac{1-\cos[k(b-a)\Delta x]}{(b-a)\Delta x}\frac{\partial W_{a,b}}{\partial x_a}\right\}$$
$$\times\,\omega_{\rm SPH,AV}-\omega^2_{\rm SPH}=0. \qquad (59)$$

Equation (59) has an extra term relative to equation (51), and the root of the equation is given by

$$\omega_{\rm SPH,AV}=\frac{{\rm i}b_{\rm SPH,AV}\pm\sqrt{-b^2_{\rm SPH,AV}+4\omega^2_{\rm SPH}}}{2}, \qquad (60)$$

where $b_{\rm SPH,AV}$ is $M\frac{c_s}{\rho_0}\alpha h\sum_b\frac{1-\cos[k(b-a)\Delta x]}{(b-a)\Delta x}\frac{\partial W_{a,b}}{\partial x_a}$.

The artificial viscosity gives not only a phase difference but also a damping to the system because the imaginary term, $b_{\rm SPH,AV}$, is always negative. E_Φ and $E_{\rm R}$ from equation (60) are shown in Figs 3 and 4, respectively. Note that there is an unstable region in the contours of E_Φ, where the argument of the square root in equation (60) is negative.

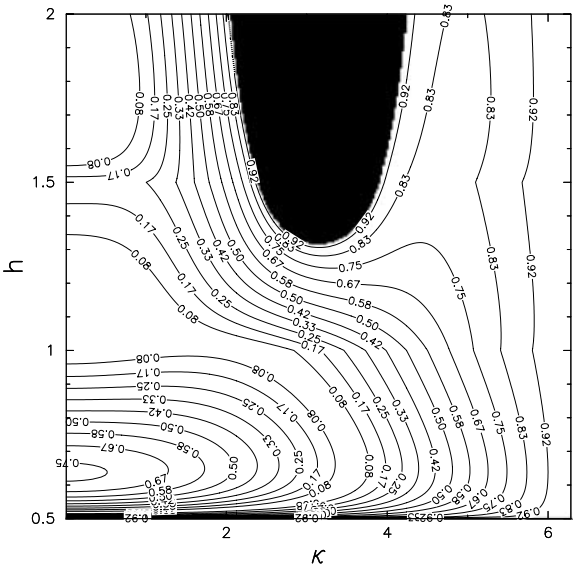

Figure 3. Phase error contours for isothermal SPH with artificial viscosity. α is set to 1. The region filled by black in the upper to middle area is the unstable region. In this region, $\omega^2_{\rm SPH,AV}$ is smaller than 0.

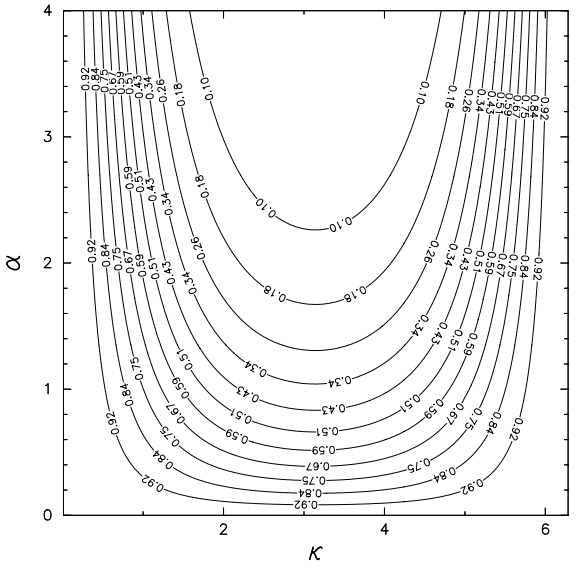

Figure 4. Amplitude error contours for isothermal SPH with artificial viscosity on the (κ, α) plane. $b_{\rm SPH,AV}$ is always negative, so the amplitude of the initial perturbation decays with time. The contours show the values at the time, $t = 1$, i.e. just after one period of the wave. The amplitude error depends very weakly on α in the stable region. This means that provided α is set in the stable region, the value of α is not very critical.

4.3 GPH

The isothermal Riemann problem has a functional form for P^* given by equation (27), and its linearized form is

$$P^*\left(\frac{1}{\rho_a^2}+\frac{1}{\rho_b^2}\right)=\frac{c_s}{\rho_0}\left[(\delta v_a-\delta v_b)+2c_s-\frac{c_s}{\rho_0}(\delta\rho_a+\delta\rho_b)\right]$$
$$=\frac{c_s}{\rho_0}\left[V{\rm e}^{{\rm i}\phi_a}(1-{\rm e}^{{\rm i}\phi_{b-a}})+2c_s\right.$$
$$\left.-\frac{c_s}{\rho_0}R{\rm e}^{{\rm i}\phi_a}(1+{\rm e}^{{\rm i}\phi_{b-a}})\right]. \qquad (61)$$

With equations (43), (44) and (61), the dispersion relation of isothermal GPH becomes

$$\omega^2_{\rm GPH}=M\frac{c_s^2}{\rho_0}\sum_b\left\{-\frac{M}{\rho_0}\left[\sum_b(1-{\rm e}^{{\rm i}\phi_{b-a}})\frac{\partial W_{a,b}}{\partial x_a}\right]\right.$$
$$\left.\times(1+{\rm e}^{{\rm i}\phi_{b-a}})\frac{\partial W_{a,b}}{\partial x_a}+2(1-{\rm e}^{{\rm i}\phi_{b-a}})\frac{\partial^2 W_{a,b}}{\partial x_a^2}\right\}$$
$$-M\frac{c_s}{\rho_0}\sum_b(1-{\rm e}^{{\rm i}\phi_{b-a}})\frac{\partial W_{a,b}}{\partial x_a}\omega{\rm i}. \qquad (62)$$

Equation (62) can again be simplified by substituting for $\omega^2_{\rm SPH}$ from equation (51),

$$\omega^2_{\rm GPH}+M\frac{c_s}{\rho_0}\sum_b\left\{\sin[k(b-a)\Delta x]\frac{\partial W_{a,b}}{\partial x_a}\right\}\omega_{\rm GPH}-\omega^2_{\rm SPH}=0, \qquad (63)$$

and $\omega_{\rm GPH}$ is then

$$\omega_{\rm GPH}=\frac{-b_{\rm GPH}\pm\sqrt{b^2_{\rm GPH}+4\omega^2_{\rm SPH}}}{2}, \qquad (64)$$

Downloaded from https://academic.oup.com/mnras/article/340/1/73/1130605 by guest on 12 November 2025

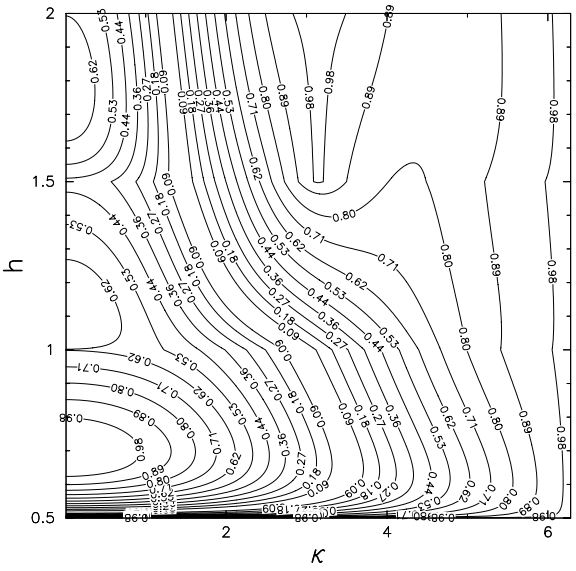

Figure 5. Phase error contours for isothermal GPH. At all wavelengths, $\omega^2_{\rm GPH}$ is positive, and the general trend is similar to the case of SPH without artificial viscosity.

where $b_{\rm GPH}$ is $M\frac{c_{\rm s}}{\rho_0}\sum_b \sin[k(b-a)\Delta x]\frac{\partial W_{a,b}}{\partial x_a}$. $\omega_{\rm GPH}$ has no imaginary part, so GPH does not give any damping to the system. Furthermore, $\omega^2_{\rm GPH}$ is always positive, so there is no unstable region. The phase error of isothermal GPH is shown in Fig. 5.

5 TESTS

Here we describe eight tests. The first four demonstrate that GPH can treat sound and shock waves at least as well as SPH. The next three show that GPH can also handle strong rarefaction waves, that GPH does not suffer from penetration and that GPH can handle shear properly. The final test shows the overall performance of GPH.

5.1 Description of an isothermal sound wave

To verify the errors discussed in the previous section, numerical calculations of sound wave propagation have been performed. Initially, the system is homogeneous, and a Gaussian velocity perturbation is given in the centre of the system. The amplitude of the perturbation is 0.01 in terms of the isothermal speed of sound. The perturbation propagates at the isothermal speed of sound (which is set to 1.0), and the wave is reflected at the boundary of the system because we have used a mirror boundary condition.

We have performed this test for cases 1–4 of GPH and for SPH, and there are no major differences between the results for the different versions of GPH. This is the reason why we presume that the stability of case 4 is the same as cases 1–3. Figs 6–10 show the results for each version of GPH and for SPH. The results for GPH look better than those for SPH, because the distortion of the wave is less serious with GPH. We have used constant h in this test. Note that GPH is only first order in time while SPH is second order in time.

5.2 The shock tube test (Sod test)

The shock tube problem is widely used to test the performance of numerical codes (Sod 1978). There are five distinct regions in this test, and four boundaries separating these regions. The performance of numerical codes can be estimated by comparing the numerical and analytic results at the boundaries.

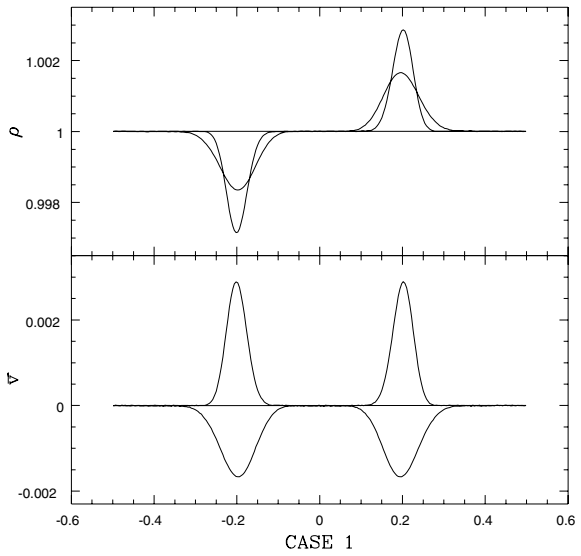

Figure 6. The isothermal sound wave propagation test for GPH case 1. These are density and velocity profiles. Positive velocity means propagation away from the centre and negative velocity means propagation towards the centre. Each wave is shown at two times, $t = 0.2$ and 0.8. The shape of the wave becomes more dispersive with time, as predicted by the stability analysis. Each wave component of the initial perturbation propagates with a different velocity. This is the reason why the shape of the wave is distorted.

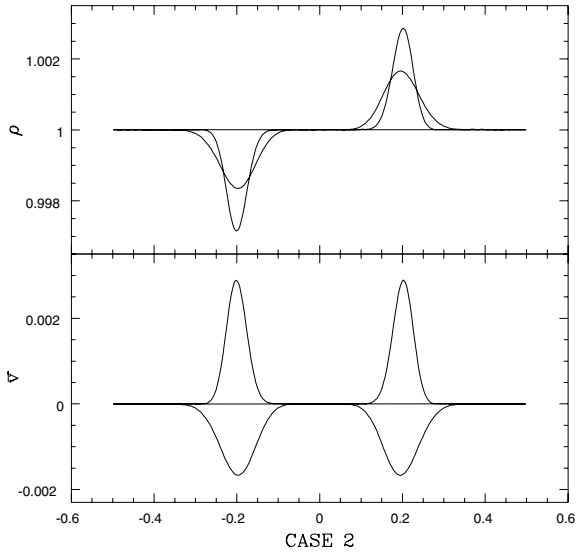

Figure 7. The isothermal sound wave propagation test for GPH case 2.

5.2.1 Initial conditions

The initial conditions shown in Table 1 are used in the shock tube tests. The calculation domain is divided into two parts, and the left-hand side is hotter and denser than the right-hand side. There is one rarefaction wave and one shock wave in this test. γ is set to 1.4 and $t_{\rm end}$ is 0.17. 250 (200 + 50) particles have been used in this test.

Downloaded from https://academic.oup.com/mnras/article/340/1/73/1130605 by guest on 12 November 2025

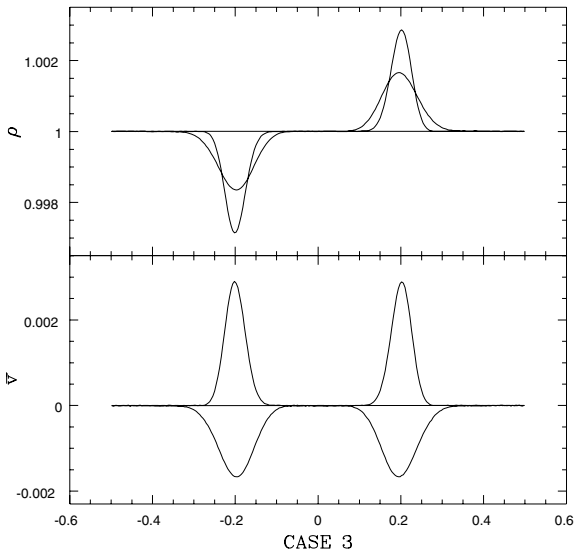

Figure 8. The isothermal sound wave propagation test for GPH case 3.

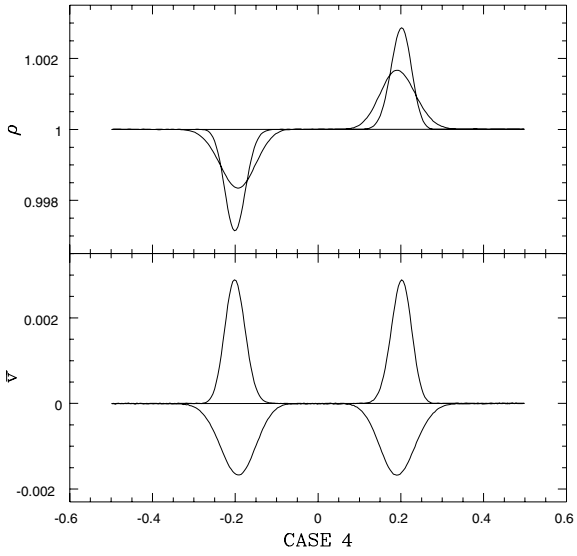

Figure 9. The isothermal sound wave propagation test for GPH case 4.

5.2.2 *Results*

Figs 11–14 show the results obtained with each version of GPH. There is no significant difference between the various versions of GPH. All numerical results reproduce the analytic solution very well. However, there is a broken feature at the contact discontinuity owing to the steep gradients there. Monaghan (1997) discusses this broken feature in detail. The broken features of cases 3 and 4 are less severe than those of cases 1 and 2. There is a smoothed feature in the vicinity of the head (and tail) of the rarefaction wave. This is a characteristic property of first-order schemes.

5.3 The strong blast wave test

The strong blast wave test is similar to the Sod test, but the pressure contrast between the left- and right-hand side is more severe than in the Sod test. There is no density contrast initially, so this test

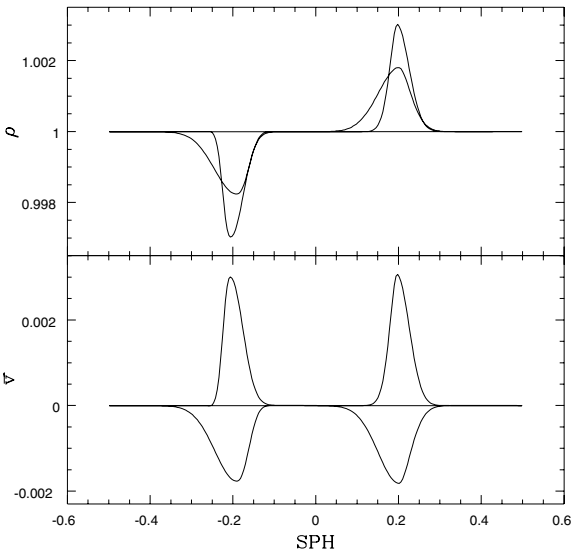

Figure 10. The isothermal sound wave propagation test for SPH. One can readily see that the distortion of SPH is larger than that of GPH. Note that SPH is second order while GPH is only first order in time.

Table 1. Initial conditions for the shock tube test. This test is described in detail in Courant & Friedrichs (1976) and Sod (1978). $\gamma = 1.4$ and $t_{\rm end} = 0.17$. 200 and 50 particles have been used on the left- and right-hand side of the contact discontinuity, respectively.

Physical properties	Left-hand side value	Right-hand side value
ρ	1.0	0.25
v	0.0	0.0
P	1.0	0.1795

describes the detailed structure of a strong blast wave propagating into a uniform density medium.

5.3.1 *Initial conditions*

The initial conditions shown in Table 2 are used in this test. The pressure contrast is 3×10^{10}. 250 particles are used. γ is set to 1.4 and $t_{\rm end}$ is 5×10^{-3}.

5.3.2 *Results*

The fluid on the left drives a strong compression wave into the fluid on the right, and this compression wave leaves a very rarefied region in its wake. The material swept-up by the strong compression wave is concentrated in a narrow region between the shock front and the contact discontinuity, so the density in this region increases dramatically. The performance of the numerical code can be evaluated by its ability to model this high-density region accurately. Figs 15–18 show the results for this test. The scaling of the density, pressure and specific internal energy in these figures is logarithmic. Although there is a smoothed feature at the head of the rarefaction wave, cases 1–4 follow the analytic solution well. The broken feature around the contact discontinuity is caused by the steep gradients in the initial conditions there.

5.4 The isothermal shock tube tests

If the cooling time-scale of a system is much shorter than the dynamical time-scale and the equilibrium temperature is independent

Downloaded from https://academic.oup.com/mnras/article/340/1/73/1130605 by guest on 12 November 2025

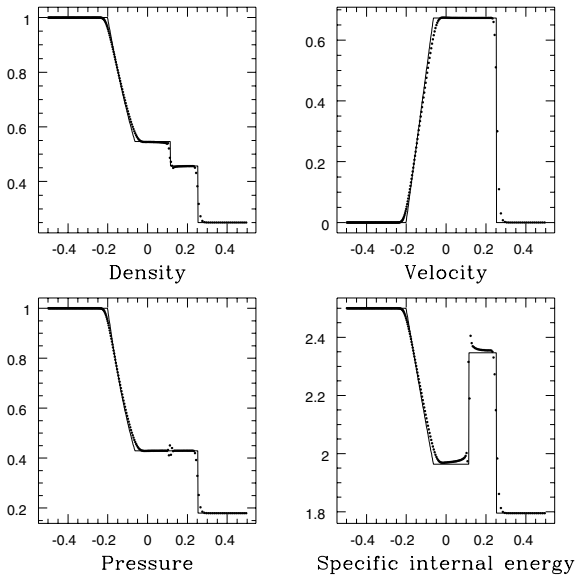

Figure 11. The shock tube test for GPH case 1. All the major features (including the rarefaction wave, the contact discontinuity and the shock wave) follow very well the analytic solution represented by the solid line (dots are the numerical results). There is a broken feature at the contact discontinuity, and this is caused by the steep gradients there. There is a smoothed feature at the head of rarefaction wave, because GPH is a first-order scheme.

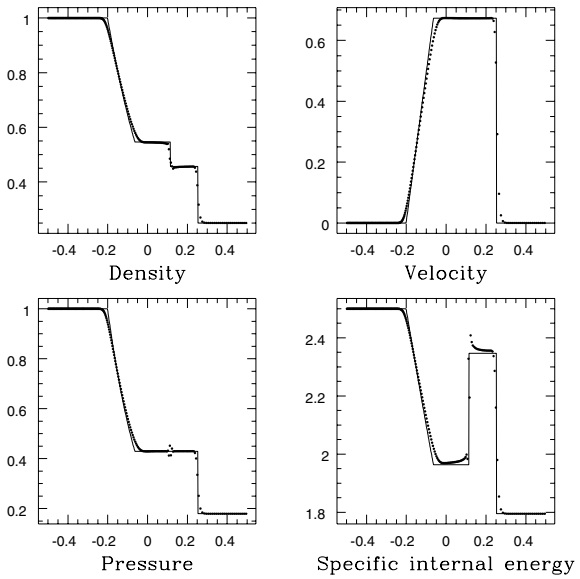

Figure 12. The shock tube test for GPH case 2. This is very similar to the results for case 1.

of the density, one can assume that the system is isothermal. This is often a good approximation in the interstellar medium. The early stages of cloud contraction are also a good example of isothermal hydrodynamics. In order to test the isothermal Riemann solver introduced in Section 3.3, we have performed isothermal shock tube tests. Isothermal GPH is faster than normal GPH because it uses a non-iterative Riemann solver.

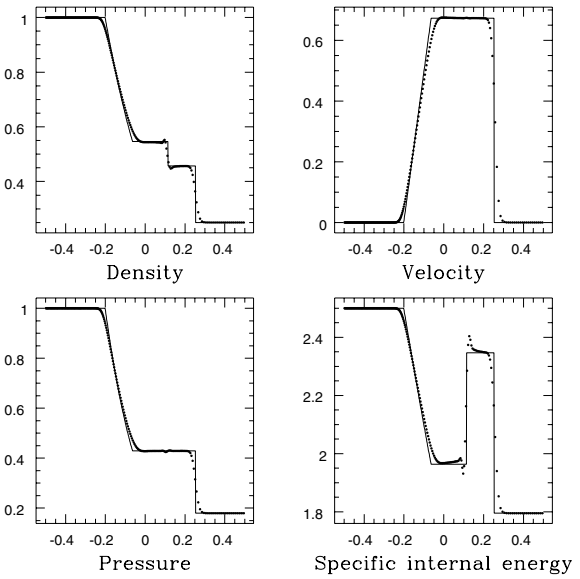

Figure 13. The shock tube test for GPH case 3. The broken feature in the vicinity of the contact discontinuity is less serious than that of case 1 (or case 2), especially in the pressure plot. There are smoothed features in the head and tail of the rarefaction wave.

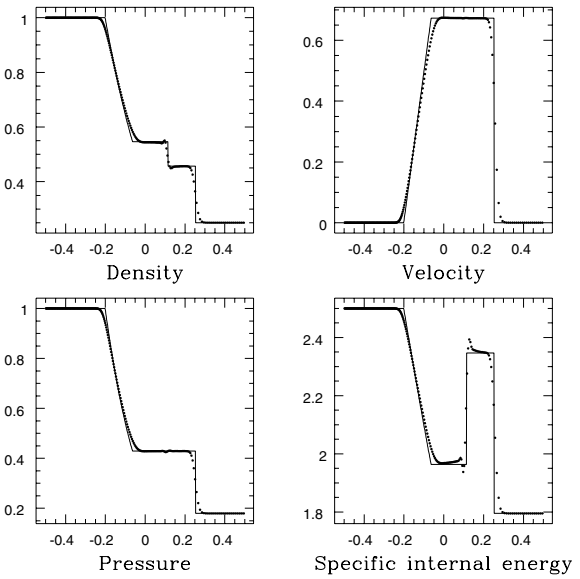

Figure 14. The shock tube test for GPH case 4. This is very similar to the results for case 3, but case 4 consumes more CPU time than case 3 (for the details of the implementation of case 4, see Inutsuka & Imaeda 2001; Cha 2002).

Table 2. Initial conditions for the strong blast wave test. This is similar to the Sod test, but more severe. 250 particles are used. γ is set to 1.4 and $t_{\rm end}$ is 5×10^{-3}. Note the high pressure contrast and the uniform density.

Physical properties	Left-hand side value	Right-hand side value
ρ	1.0	1.0
v	0.0	0.0
P	3×10^3	1×10^{-7}

Downloaded from https://academic.oup.com/mnras/article/340/1/73/1130605 by guest on 12 November 2025

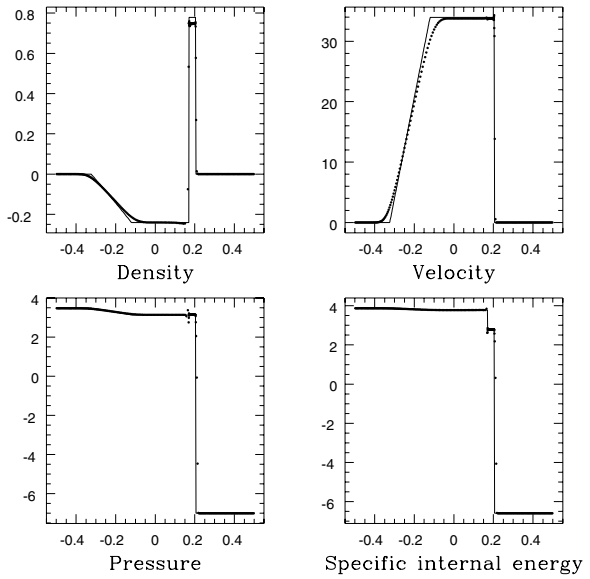

Figure 15. The strong blast wave test for GPH case 1. There is a very thin and dense region between the shock front and the contact discontinuity. Case 1 cannot describe this region exactly. The density of this region is underestimated by a few percent. Also there is a ripple in the vicinity of the contact discontinuity. The scaling of the density, pressure and specific internal energy is logarithmic.

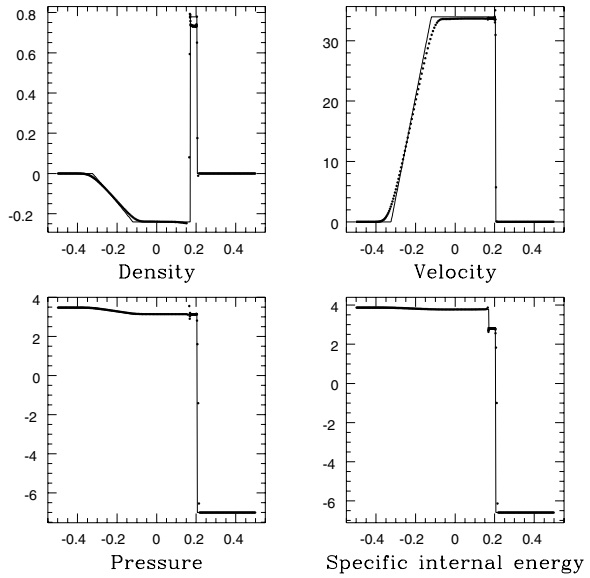

Figure 16. The strong blast wave test for GPH case 2. The density plot is worse than case 1. There is a ripple at the contact discontinuity and an overshoot at the shock front on the velocity plot.

5.4.1 Initial conditions

Initial conditions for the isothermal shock tube test are shown in Table 3. The initial conditions are very similar to those for the adiabatic Sod test, but the speed of sounds on the left- and right-hand side are the same. 250 particles are used in this test, and $t_{\rm end}$ is 0.17.

5.4.2 Results

Figs 19–22 show the results for this test. The major difference between the adiabatic and isothermal shock tube tests is the density profile. There is no density change across the contact discontinuity in the isothermal shock tube test. All versions of GPH show a very clean pressure profile, and there are no significant differences between the numerical and analytical solutions.

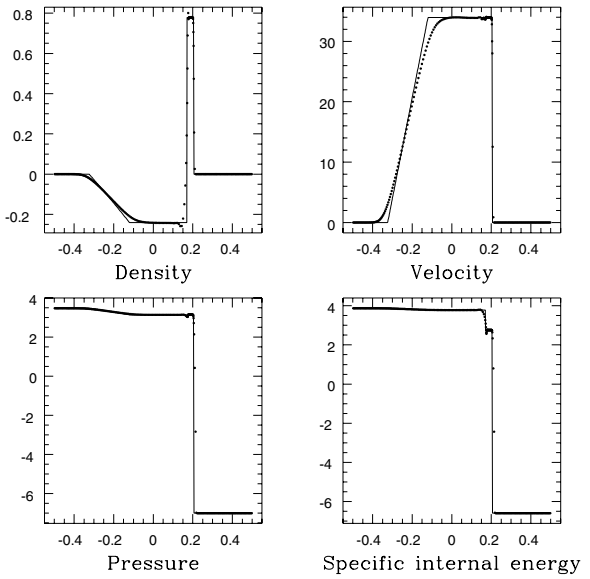

Figure 17. The strong blast wave test for GPH case 3. The density plot is better than for case 1 (or 2), and the ripple at the contact discontinuity is less severe. The shock front at $x \simeq 0.2$ is cleaner than for cases 1 or 2.

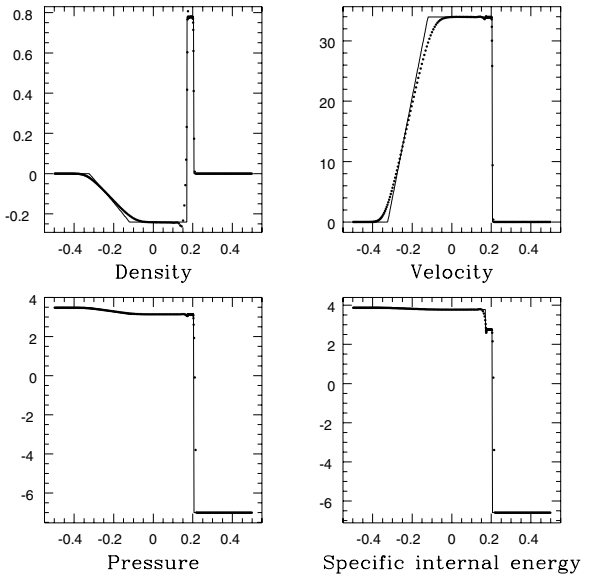

Figure 18. The strong blast wave test for GPH case 4. These results are apparently very similar to the results for case 3.

5.5 The Sjögreen test for low-density flows

The iterative Riemann solver described in Section 3.2 sometimes fails to find P^* (or v^*) in very low-density flows. If there are two strong rarefaction waves (or one rarefaction wave), then a very low-density region (fluid cavity) is created, and the iterative Riemann solver diverges. The divergence may occur in the middle of iteration or in the first estimate of P^*.

Godunov (1959) (see also Richtmyer & Morton 1967) has a prescription to fix this problem. According to Godunov's prescription,

Downloaded from https://academic.oup.com/mnras/article/340/1/73/1130605 by guest on 12 November 2025

Table 3. Initial conditions for the isothermal shock tube test. The isothermal speed of sound ($\equiv \sqrt{P/\rho}$) should be constant throughout the calculation domain. 250 particles are used in this test, and $t_{\rm end}$ is 0.17.

Physical properties	Left-hand side value	Right-hand side value
ρ	1.0	0.25
v	0.0	0.0
P	1.0	0.25

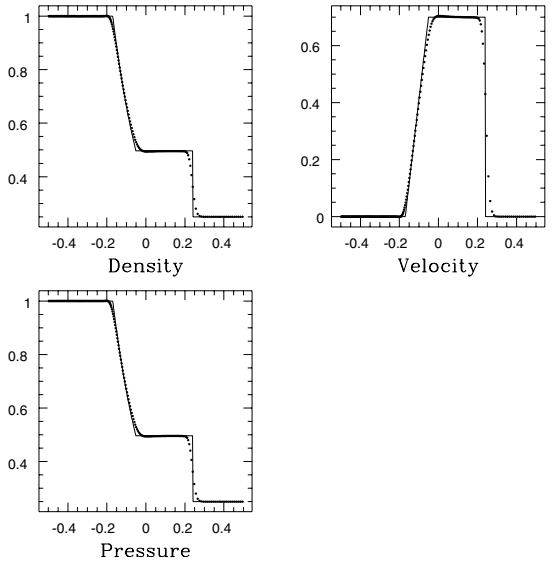

Figure 19. The isothermal shock tube test for GPH case 1. There is no significant difference between the numerical result and the analytic solution.

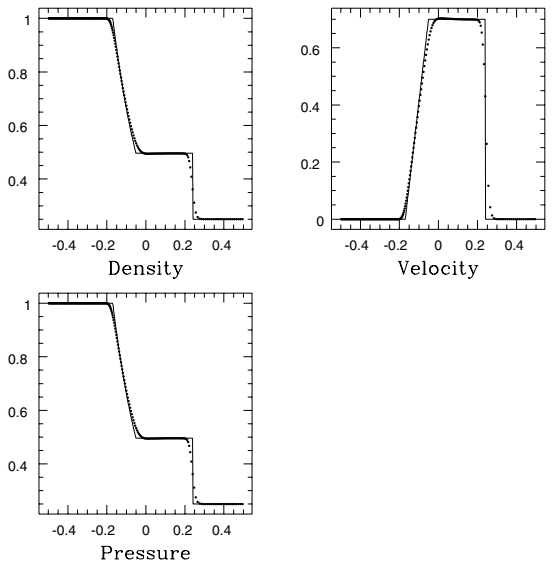

Figure 20. The isothermal shock tube test for GPH case 2.

in the case of divergence (which is a very rare occurrence), the pressure value, P^*, should be replaced with another value. The replacement is explained in detail in Richtmyer & Morton (1967).

Another possible solution to this problem is to use non-iterative Riemann solvers (Dukowicz 1985; Dai & Woodward 1995; Roe 1997) or to add pressure protection to prevent negative values of P^*

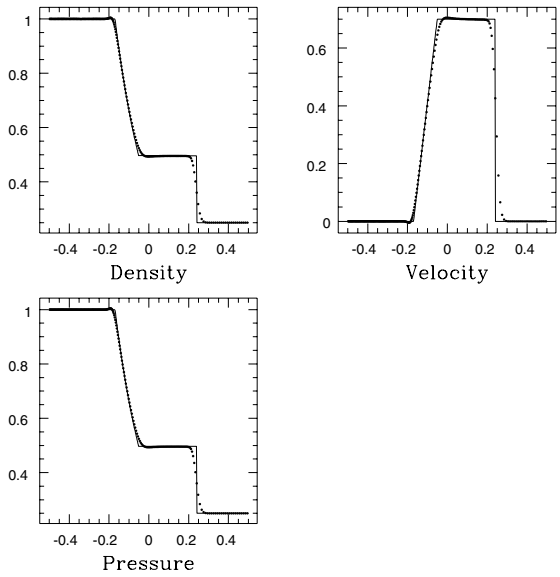

Figure 21. The isothermal shock tube test for GPH case 3.

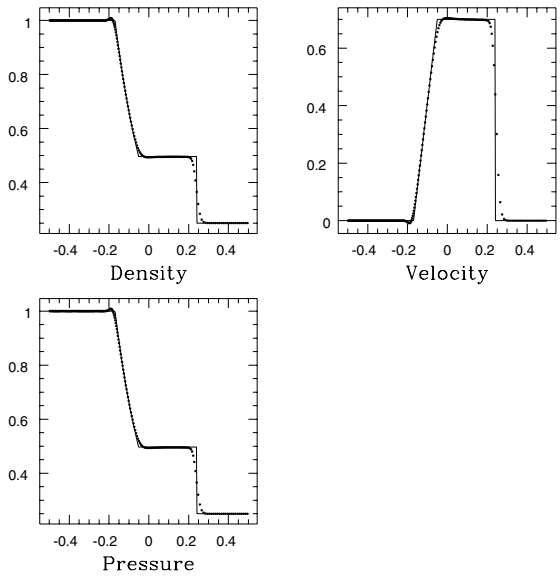

Figure 22. The isothermal shock tube test for GPH case 4.

Table 4. Initial conditions for the Sjögreen test. There is no contrast in the density and pressure, but the two fluids are moving away from each other. Consequently, a very low-density region is created in the vicinity of the initial contact front. The iterative Riemann solver sometimes fails to find P^* (or v^*) in this situation. A special treatment is needed to fix this divergence, and this test shows the effect of this treatment. $\gamma = 1.4$ and $t_{\rm end} = 0.18$.

Physical properties	Left-hand side value	Right-hand side value
ρ	1.0	1.0
v	−2.0	2.0
P	0.4	0.4

(van Leer 1997). We have used the pressure protection method in all versions of GPH.

In order to examine GPH in a very low-density situation, we have performed the test of two rarefaction waves that are moving

Downloaded from https://academic.oup.com/mnras/article/340/1/73/1130605 by guest on 12 November 2025

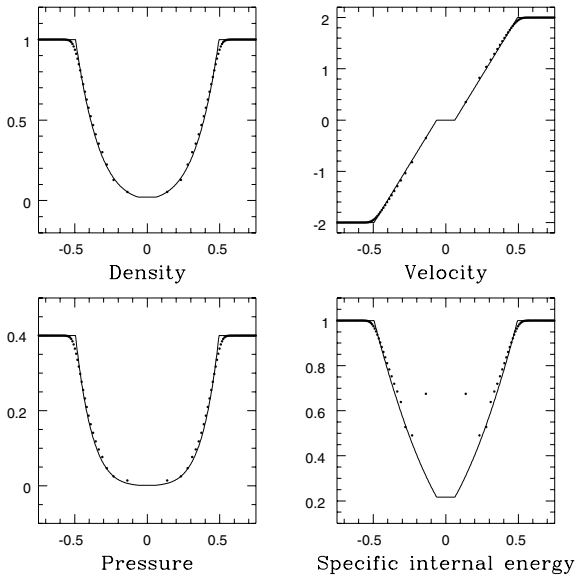

Figure 23. The Sjögreen test for GPH case 1. The iterative Riemann solver with pressure protection works well in the very low-density region owing to the receding fluids. However, there is an error in the vicinity of $x = 0$ (initial contact front) on the energy plot.

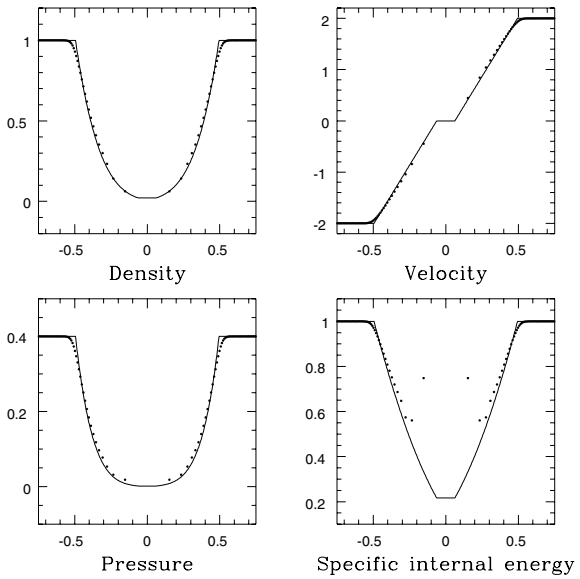

Figure 24. The Sjögreen test for GPH case 2. Note the error on the energy plot.

away from each other. This test is called the 123 test (Toro 1999) or Sjögreen test (Einfeldt et al. 1991; Monaghan 1997). There is a very low-density region in this test because of the two receding rarefaction waves, and the different versions of GPH are tested to see how well they describe the flow cavity.

5.5.1 Initial conditions

Initial conditions for the Sjögreen test are shown in Table 4. The only difference between the left- and right-hand side is the velocity. The two sides are moving away from each other to make a flow cavity. $\gamma = 1.4$ and $t_{\rm end} = 0.18$ are used in this test.

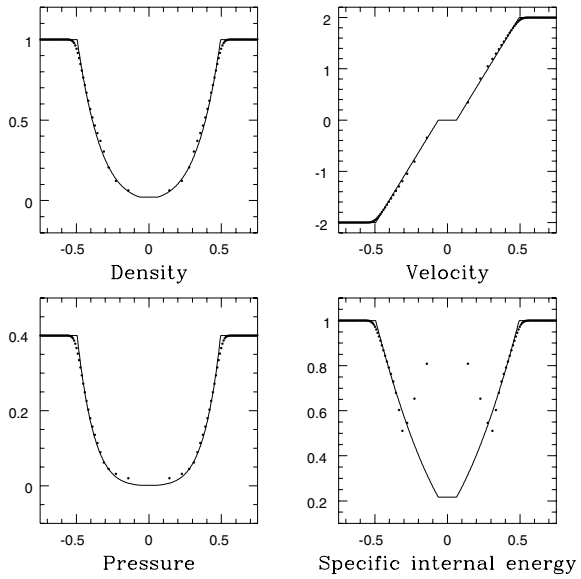

Figure 25. The Sjögreen test using GPH case 3. Note the error on the energy plot.

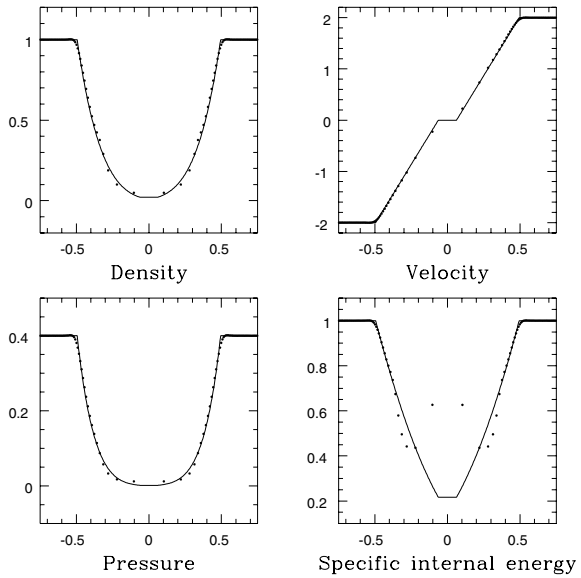

Figure 26. The Sjögreen test using GPH case 4. Note the error on the energy plot.

5.5.2 Results

Figs 23–26 show the results for this test. The divergence of the iterative Riemann solver is cured by pressure protection, and GPH is able to describe the flow cavity. However, there is a significant error in the vicinity of the initial contact front, especially on the energy plot.

We suspect that the failure of Godunov-type schemes in the flow cavity is not an incurable error. It is probably the fault of the iterative Riemann solver, in which case it might be avoided with the use of a different Riemann solver. We hope to explorer this possibility in the future.

5.6 Flow-collision test

In order to check the effectiveness of the Riemann solver used in GPH, flow-collision tests have been performed. We have also

Downloaded from https://academic.oup.com/mnras/article/340/1/73/1130605 by guest on 12 November 2025

performed an SPH calculation with the same initial conditions for comparison. Two fluids that have the same density and pressure are approaching each other. We have performed two cases. One is subsonic ($v_{\rm app}/c_{\rm s} = 0.6$), and the other is supersonic ($v_{\rm app}/c_{\rm s} = 1.2$). Here $v_{\rm app}$ and $c_{\rm s}$ are the approach velocity and speed of sound, respectively. $\alpha = 1$ and $\beta = 2$ are used in the SPH calculation. γ is 1.0. $t_{\rm end}$ is 0.05 in the supersonic case and 0.1 in the subsonic case.

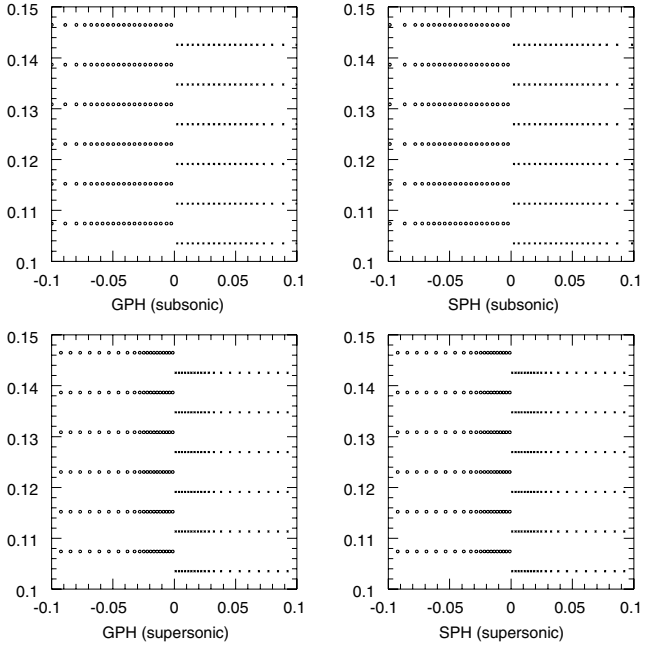

Figure 27. Subsonic (upper row) and supersonic (lower row) flow-collision tests for SPH and GPH (case 3). There is no particle penetration across the contact discontinuity in either SPH or GPH.

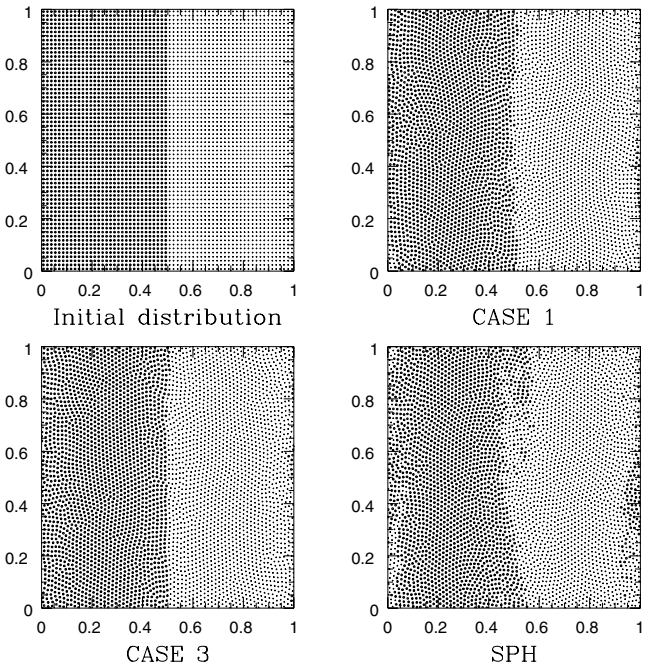

Figure 28. Test for velocity shear. The panel in the top left-hand side shows the initial conditions for this test. There is no density or pressure difference in the system, but the two fluids are moving in opposite directions along y-axis. The other panels are snapshots at $t = 6$. One can see easily that the result of GPH is better than that of SPH.

5.6.1 Results

Fig. 27 shows the results of SPH and GPH (case 3). All of them are good because there is no particle penetration. We see that the

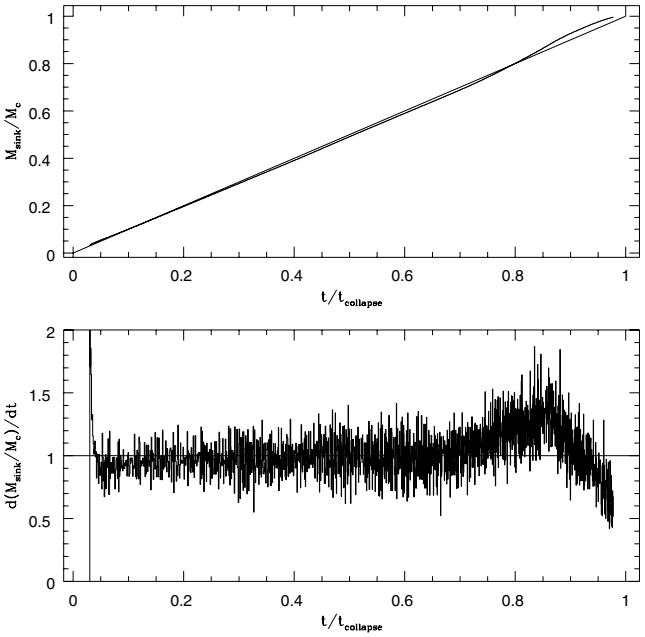

Figure 29. The growth of the mass of the central core and the mass accretion rate. Time and mass are scaled by $t_{\rm collapse}$ and $M_{\rm c}$, respectively. This is the result obtained using GPH case 3. The straight line in the upper panel is the analytic solution and the curved line is the numerical result. The numerical results diverge from the similarity solution after 0.7 $t_{\rm collapse}$, but the difference is not very large. There is no significant error in the results.

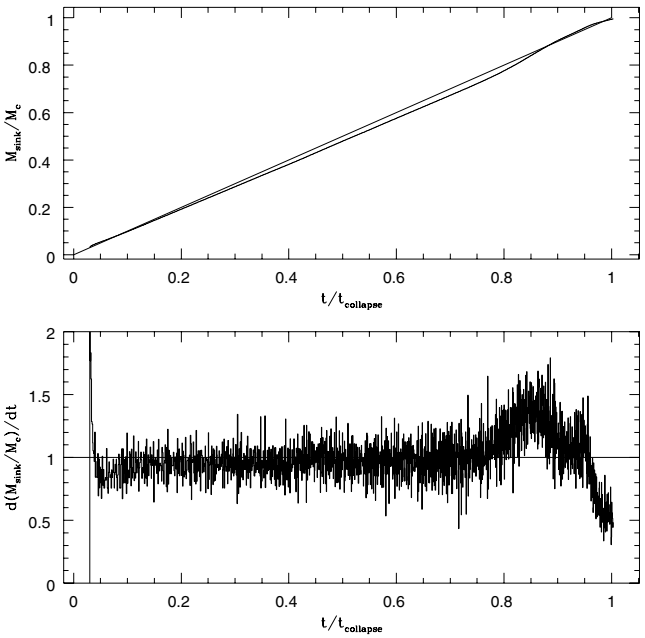

Figure 30. The same plots as in Fig. 29, but this is the result obtained using SPH. Note the bigger difference between the numerical and analytic solutions, as compared with the result using GPH.

Downloaded from https://academic.oup.com/mnras/article/340/1/73/1130605 by guest on 12 November 2025

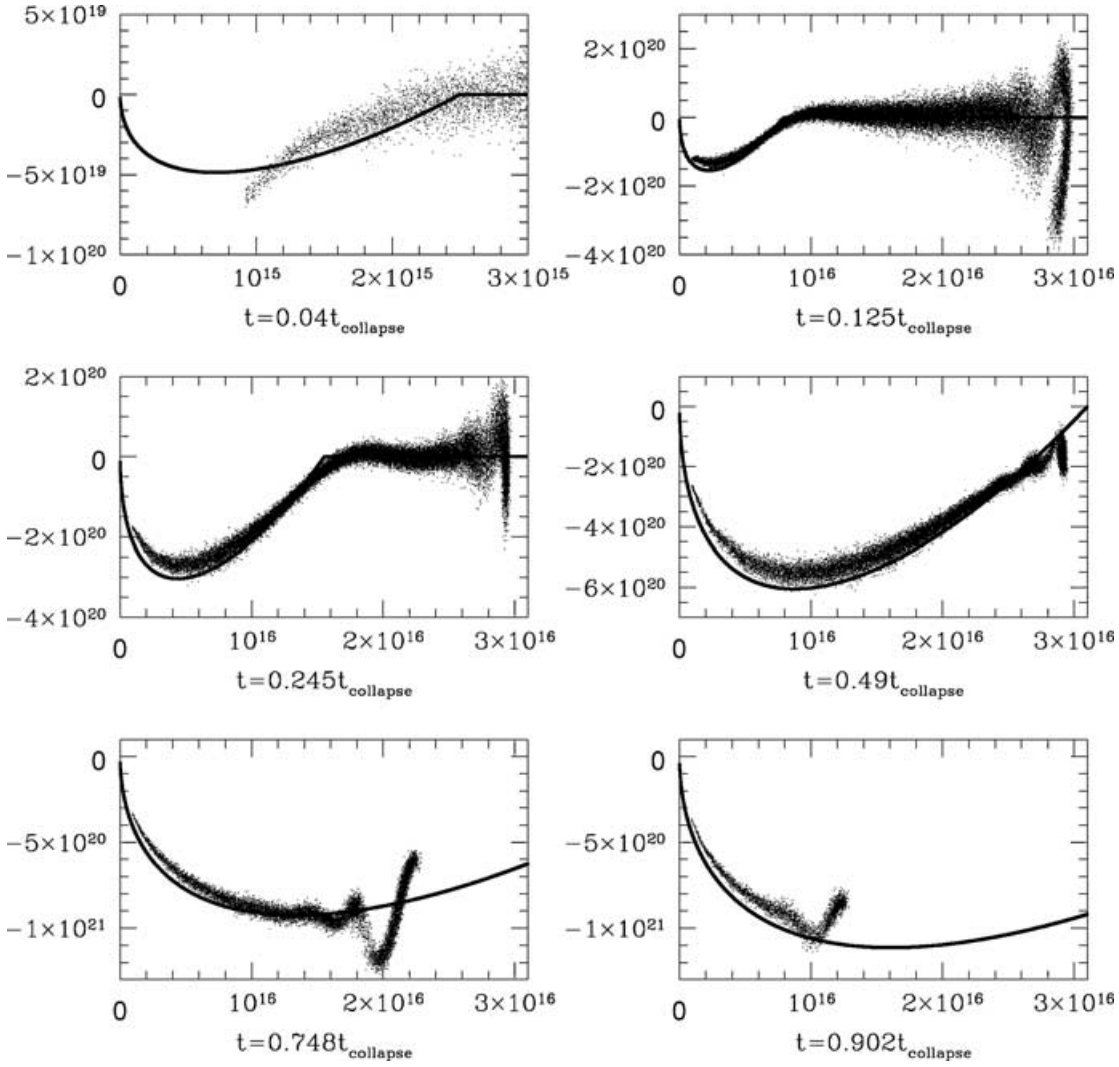

Figure 31. $\boldsymbol{r}_i \cdot \boldsymbol{v}_i$ plot obtained using GPH case 3. The big ripple in the tail is caused by the initial shrinking of the model cloud. See the text for details. Overall the analytic solution is reproduced well.

Riemann solver prevents particle penetration effectively in the subsonic and supersonic flow collision.

5.7 Test for velocity shear

Artificial viscosity is introduced in SPH to regulate shock waves. The switch to detect shock waves is $\boldsymbol{v}_{ij} \cdot \boldsymbol{r}_{ij}$. If $\boldsymbol{v}_{ij} \cdot \boldsymbol{r}_{ij}$ is less than 0, particles i and j are approaching, and the artificial viscosity is turned on. Although artificial viscosity is fairly effective for treating shock waves, it has an undesirable side-effect. If there is velocity shear, the switch turns the artificial viscosity on, even though there is no shock wave. A typical case of this situation is a differentially rotating system. The artificial viscosity is turned on unnecessarily, and brakes the differential rotation.

Table 5. Physical properties of SIS used in the test of SIS collapse. 50 000 particles have been used in this test.

Physical quantity	Value
M_c	$1.0 M_\odot$
R_c	10^{-2} pc
T_c	57.3219 K
$c_s (\equiv \sqrt{kTc/\bar{m}})$	$4.635\,86 \times 10^4$ cm s^{-1}
$\rho_{edge} [\equiv \rho(R_c)]$	$5.387\,73 \times 10^{-18}$ g cm^{-3}
$P_{edge} (\equiv c_s{}^2 \rho_{edge})$	$1.157\,89 \times 10^{-8}$ dyne cm^{-2}
R_{sink}	$0.03\ R_c$
m_0	0.975
$t_{collapse}$	$1.365\,32 \times 10^{12}$ s

In order to compare GPH and SPH in a system that has velocity shear, we have performed the following test. The top left-hand panel of Fig. 28 shows the initial conditions. There is no contrast in density and pressure, but two adjacent fluids move in opposite directions along the y-axis. The initial velocity is given by

$$(v_x, v_y) = (0, \sin 2\pi x). \tag{65}$$

Periodic boundary conditions are used in the x- and y-directions. $\alpha = 1$ and $\beta = 2$ are used in the calculation using SPH.

5.7.1 *Results*

The results at $t = 6$ are shown in Fig. 28. One can see that the result using SPH is much more disordered than that using GPH. Since in this test an inviscid flow is assumed, and since there is no initial perturbation, Kelvin–Helmholtz instability should not, strictly speaking, be expected. The reason for the generation of disorder in the SPH result is that artificial viscosity is activated unnecessarily

Downloaded from https://academic.oup.com/mnras/article/340/1/73/1130605 by guest on 12 November 2025

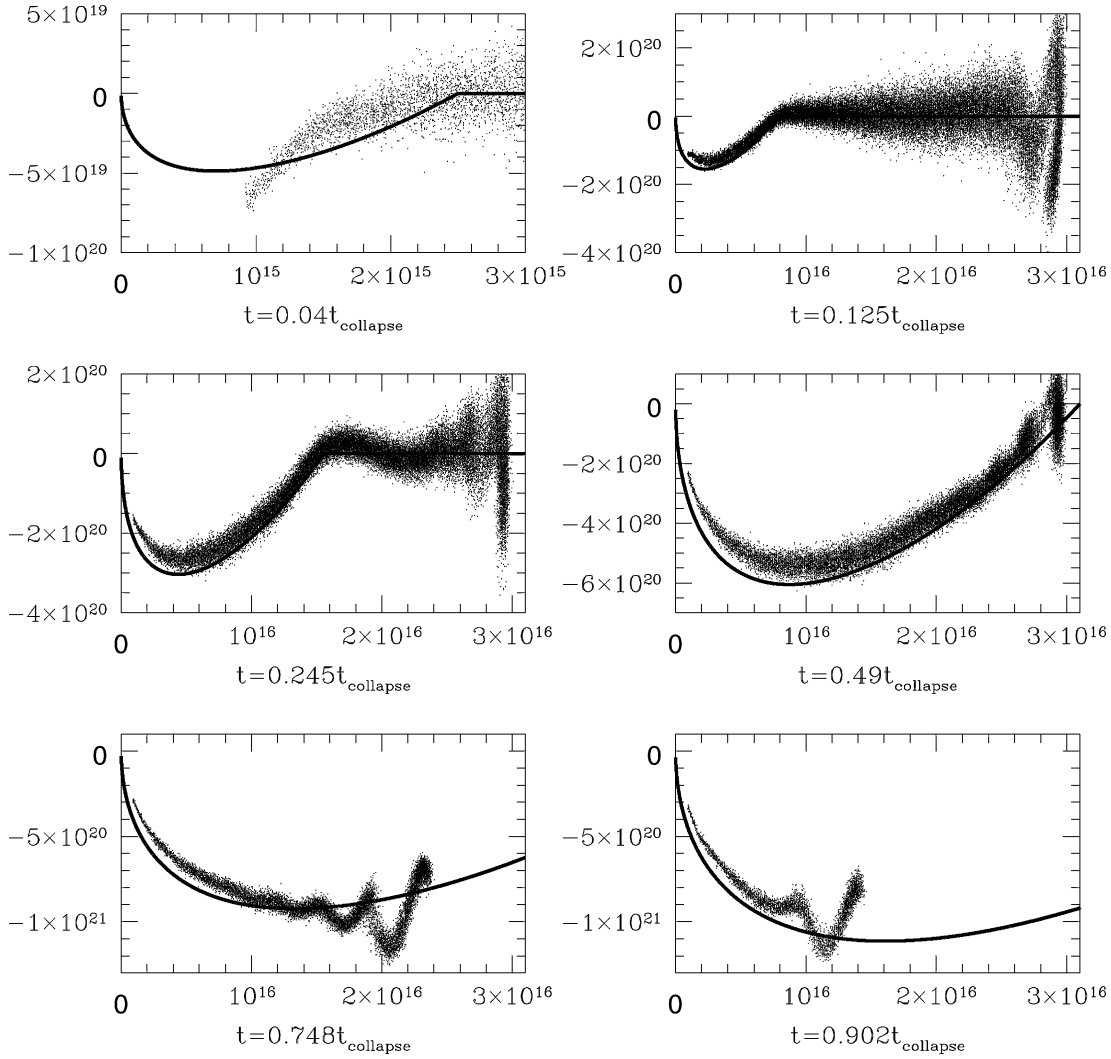

Figure 32. $\boldsymbol{r}_i \cdot \boldsymbol{v}_i$ plot obtained using SPH. This shows more dispersion than was obtained using GPH.

by the velocity shear. Much less disorder is generated in the GPH result because the Riemann solver gives rise to much less numerical diffusion. In a companion paper (Cha & Whitworth 2003) we report several GPH simulations of rotating cloud collapses, including initial conditions that involve differential rotation. In all cases the spurious transport of angular momentum is negligible.

5.8 Collapse of a singular isothermal sphere

GPH is composed of many parts, not only the Riemann solver but also the variable-h sizing routine, the gravity calculation and so on. A tree-code is also an essential part of GPH. In order to verify the real performance of GPH, a three-dimensional astrophysical problem should be performed. We have performed the collapse of a singular isothermal sphere (SIS), and compared the result with the analytic solution derived by Shu (1977).

5.8.1 Initial condition

The SIS is the limiting case of an isothermal sphere. It has an infinite density at its centre, and its internal structure is given by

$$\rho(r) = \frac{c_s^2}{2\pi G} r^{-2}, \quad M(r) = \frac{2c_s^2}{G} r. \tag{66}$$

The collapse of an SIS is described by the 'expansion wave solution' given by Shu (1977). We will omit a detailed description of this solution. The physical quantities and the initial configuration for the SIS collapse test are given in Table 5. 50 000 particles have been used in the test. The SIS has a singular point at the centre, and the singular point is represented by a sink particle (see Bate, Bonnell & Price 1995 and Cha 2002 for details of how sink particles are treated).

The SIS is in hydrostatic equilibrium, but it has a larger dimensionless radius $\xi(=\infty)$ than the $\xi(=6.45)$ of the limiting stable Bonnor–Ebert sphere (Bonnor 1956; Ebert 1956). Therefore, if there is a perturbation in the central region (Shu 1977 suggests molecule formation, for example), it starts collapsing. The singular point at the centre has infinite density, but it has finite mass. m_0 in Table 5 shows the dimensionless mass of the singular point.

5.8.2 Results

Figs 29–34 show the results of the collapse of the SIS performed using GPH (case 3) and SPH. Solid lines represent the similarity solution found by Shu (1977) and dots are the numerical results.

Figs 29 and 30 show the mass of the central core (the mass of the sink particle in the centre) and the mass accretion rate. The SIS has

Downloaded from https://academic.oup.com/mnras/article/340/1/73/1130605 by guest on 12 November 2025

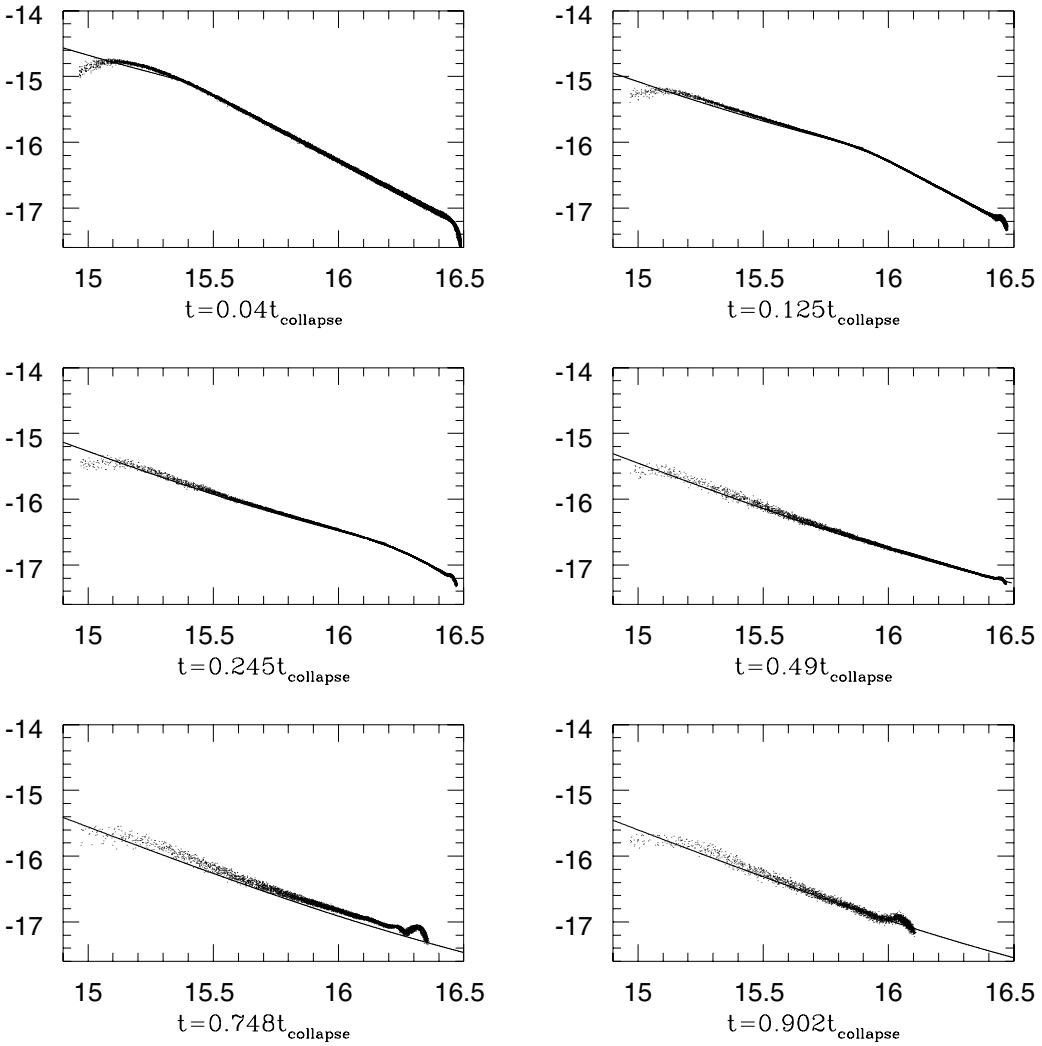

Figure 33. Density plots obtained using GPH case 3. The numerical results agree well with the analytic solution. The scaling of each axis is logarithmic.

a constant accretion rate during $t_{\rm collapse} = GM_{\rm c}/m_0 c_{\rm s}^3$, where $M_{\rm c}$ is the mass of the SIS. The numerical results reproduce the analytic solution well. Our model cloud has a finite radius, so the later part of the plot cannot follow the analytic solution. There is no gross difference between the results of SPH and GPH, but the results of GPH are closer to the analytic solution.

Figs 31 and 32 show $\boldsymbol{r}_i \cdot \boldsymbol{v}_i$. The big ripple in the outer part is caused by the initial shrinking of the model cloud. GPH shows less dispersion than SPH, especially at the head of the rarefaction wave.

Figs 33 and 34 show the density profiles obtained using GPH and SPH. The scaling is logarithmic. There is no significant error in the results.

6 DISCUSSION AND SUMMARY

We have described GPH, a new hybrid scheme combining SPH with a Godunov-type upwind scheme. Von Neumann stability analyses have been performed for isothermal SPH and GPH, and the results show that GPH is always stable at all wavelengths. Various tests have also been performed using GPH and SPH. The test results show that GPH can describe shock waves without artificial viscosity. The tests also show that particle penetration does not occur in GPH. Furthermore, GPH shows better results than SPH in a problem with velocity shear. In order to fix the divergence of the iterative Riemann solver in divergent flows, we have used a simple pressure protection algorithm. With this pressure protection, GPH appears able to describe very low-density flows.

There appears to be very little difference between the four different implementations of GPH that we have described and tested here. The inference is that the different implementations are essentially equivalent, at least as far as the tests that we have preformed here are concerned. We have a small preference for case 3, on the basis of the strong blast-wave test (Section 5.3), but we cannot be certain that a new test might not favour one of the other implementations.

GPH has other advantages beyond those described above. GPH uses a one-dimensional Riemann solver only. It is extremely hard to make multidimensional Riemann solvers (Dai & Woodward 1995, 1997; Schecter, Marchesin & Plohr 1996; Monaghan 1997). Therefore, most multidimensional upstream schemes use a one-dimensional Riemann solver, with the operator splitting method (e.g. Press et al. 1992), i.e. a one-dimensional Riemann solver is used in each direction successively. However, in GPH, all hydrodynamical interactions between particles are calculated on the line joining the particles, and so no multidimensional treatment is needed.

GPH inherits the Lagrangian nature of SPH, so Eulerian remapping processes are unnecessary, while multidimensional FDMs have

Downloaded from https://academic.oup.com/mnras/article/340/1/73/1130605 by guest on 12 November 2025

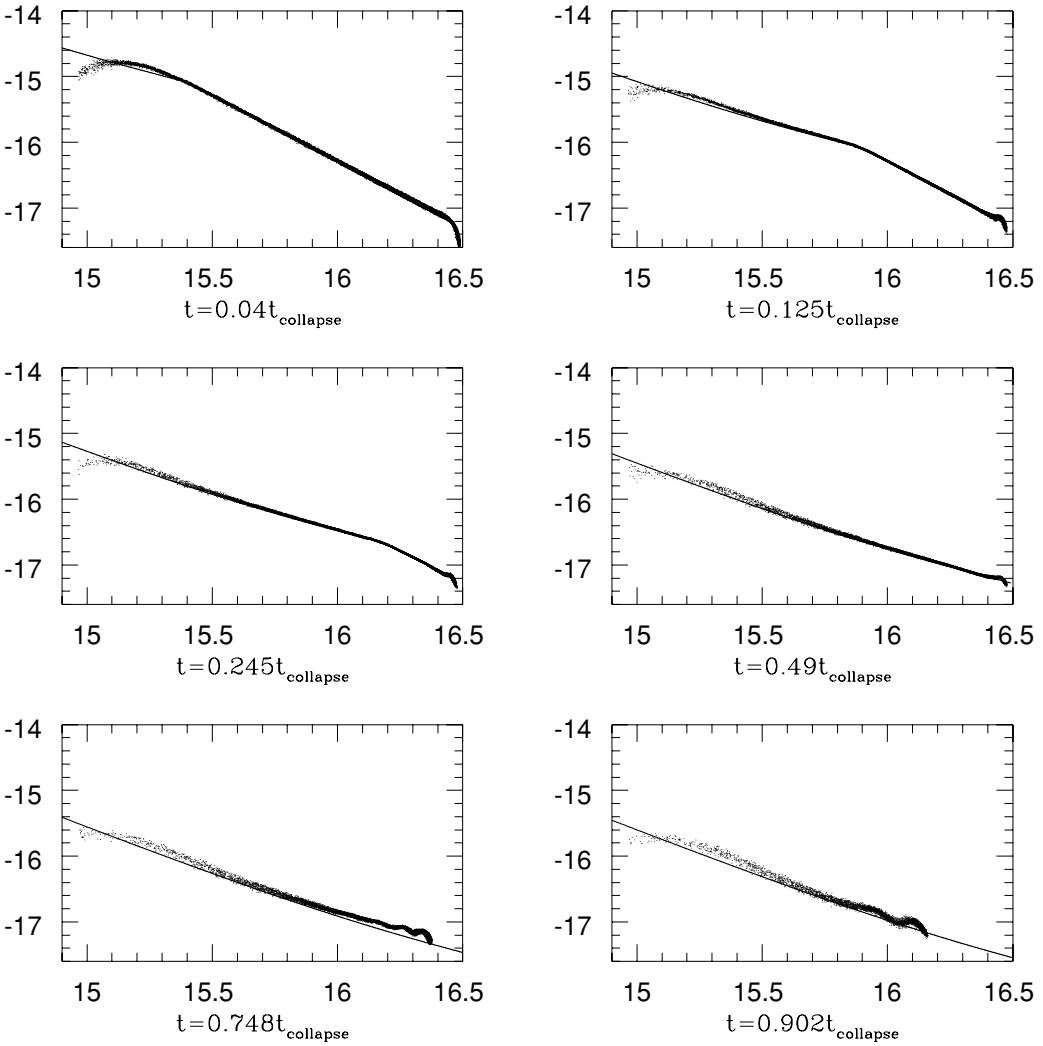

Figure 34. Density plots obtained using SPH.

to include a Eulerian remapping process. The Eulerian remapping process is a quite expensive part of multidimensional FDMs.

GPH is free from any geometrical effects because it is a grid-free Lagrangian scheme. Eulerian grid methods have some difficulties in curvilinear coordinate systems, for example, curvature effects, errors along the axes and at the origin, and inconsistency of the centre of volume and mass (Mönchmeyer & Müller 1989; Icke 1991; Blondin & Lufkin 1993). GPH avoids these problems automatically.

We also note that *both* the four implementations of GPH that we have described and tested here, *and* the SPH code that we have used for comparison, use multiple particle time-steps. However, whereas the SPH code used for comparison is second order in time (as are all the stable SPH codes of which we are aware), the implementations of GPH are only first order in time. Therefore, the extra CPU overhead arising from the Riemann solver in GPH is more than offset by the need to perform twice as many treewalks (looking for neighbours) in SPH. Consequently, GPH only takes approximately 70 percent of the CPU time of standard SPH for the same problem. The performance of the Godunov scheme is determined by the efficiency of the Riemann solver used. There has been considerable progress in solving the Riemann problem mathematically, and many methods have been proposed, including both approximate and exact Riemann solvers (Dukowicz 1985; Toro 1989; Dai & Woodward 1995; Schecter et al. 1996; Tabak 1996; Toumi & Kumbaro 1996; Ivings, Causon & Toro 1998; Roe 1997).

GPH is easily implemented from SPH by simple replacement of the artificial viscosity with a Riemann solver, and shows equal or better performance in a variety of tests.

REFERENCES

Balsara D.S., 1994, ApJ, 420, 197
Balsara D.S., 1995, J. Comp. Phys., 121, 357
Bate M.R., Bonnell I.A., Price N.M., 1995, MNRAS, 277, 362
Blondin J.M., Lufkin E.A., 1993, ApJS, 88, 589
Bonnor W.B., 1956, MNRAS, 116, 351
Cha S.-H., 2002, PhD thesis, Cardiff Univ.
Cha S.-H., Whitworth A.P., 2003, MNRAS, 340, 91
Courant R., Friedrichs K.O., 1976, Supersonic Flow and Shock Waves. Springer-Verlag, New York
Dai W., Woodward P.R., 1995, J. Comp. Phys., 121, 51
Dai W., Woodward P.R., 1997, J. Comp. Phys., 134, 261
Dukowicz J.K., 1985, J. Comp. Phys., 61, 119
Ebert R., 1956, Zs. Ap., 37, 217
Einfeldt B., Munz C.D., Roe P.L., Sjögreen B., 1991, J. Comp. Phys., 92, 273

Downloaded from https://academic.oup.com/mnras/article/340/1/73/1130605 by guest on 12 November 2025

Gingold R., Monaghan J.J., 1977, MNRAS, 181, 375
Gingold R.A., Monaghan J.J., 1982, J. Comp. Phys., 46, 429
Godunov S.K., 1959, Zh. Vychisl. Mat. Mat. Fiz., 47, 271
Godunov S.K., 1999, J. Comp. Phys., 153, 6
Hirsch C., 1989, Numerical Computation of Internal and External Flows, 1st edn. John Wiley and Sons, Brussels
Hirsch C., 1997, J. Comp. Phys., 135, 227
Icke V., 1991, A&A, 251, 369
Inutsuka S.-I., 1994, in Mem. S.A. It., Vol. 65, pp. 1027–1031
Inutsuka S.-I., 1999, in Shoken M., Miyama Kohji Tomisaka T.H., eds, Astrophysics and Space Science Library, Vol. 240, Numerical Astrophysics, Proc. Int. Conf. on Numerical Astrophysics 1998, NAP98. Kluwer, Dordrecht, pp. 367–374
Inutsuka S.-I., Imaeda Y., 2001, Comp. Fluid Dynam. J., 9, 316
Ivings M.J., Causon D.M., Toro E.F., 1998, Int. J. Numer. Methods Fluids, 28, 395
Landau L., Lifshitz E., 1998, Fluid Mechanics, 2nd edn. Butterworth-Heinemann, Oxford
Lucy L.B., 1977, AJ, 82, 1013
Monaghan J.J., 1989, J. Comp. Phys., 82, 1
Monaghan J.J., 1992, A&AR, 30, 543
Monaghan J.J., 1997, J. Comp. Phys., 136, 298
Monaghan J., 2002, astro-ph/0204118
Monaghan J.J., Lattanzio J.C., 1984, Publ. Astron. Soc. Aust., 5, 493
Mönchmeyer R., Müller E., 1989, A&A, 88, 594
Morris J.P., 1996a, PhD thesis, Monash Univ.
Morris J.P., 1996b, Publ. Astron. Soc. Aust., 13, 97
Morris J.P., Monaghan J.J., 1997, J. Comp. Phys., 136, 41
Press W.H., Teukolsky S.A., Vettering W.T., Flannery B.P., 1992, Numerical Recipes, 2nd edn. Cambridge Univ. Press, Cambridge
Richtmyer R.D., Morton K.W., 1967, in L. Bers R., Courant J.J.S., eds, Difference Methods for Initial-Value Problems, 2nd edn, Interscience Tracts in Pure and Applied Mathematics No. 4 Wiley, New York
Roe P.L., 1997, J. Comp. Phys., 135, 250
Schecter S., Marchesin D., Plohr B.J., 1996, J. Diff. Eqn., 126, 303
Shu F.H., 1977, ApJ, 214, 488
Sod G.A., 1978, J. Comp. Phys., 27, 1
Springel V., Hernquist L., 2002, MNRAS, 333, 649
Tabak E.G., 1996, J. Comp. Phys., 124, 383
Toro E.F., 1989, Int. J. Numer. Methods Fluids, 9, 1145
Toro E.F., 1999, Riemann Solvers and Numerical Methods for Fluid Dynamics, 2nd edn. Springer-Verlag, Berlin
Toumi I., Kumbaro K., 1996, J. Comp. Phys., 124, 286
van Leer B., 1997, J. Comp. Phys., 135, 229
van Leer B., 1999, J. Comp. Phys., 153, 1
von Neumann J., Richtmyer R.D., 1950, J. Appl. Phys., 21, 232
Watkins S.J., Bhattal A.S., Francis N., Turner J.A., Whitworth A.P., 1996, A&AS, 119, 177
Whitehurst R., 1995, MNRAS, 277, 655
Wood D., 1981, MNRAS, 194, 201

This paper has been typeset from a TEX/LATEX file prepared by the author.

Downloaded from https://academic.oup.com/mnras/article/340/1/73/1130605 by guest on 12 November 2025